

1 Mountain permafrost in the Central Pyrenees: insights from  
2 the Devaux ice cave

3 Miguel Bartolomé<sup>1\*</sup>, Gérard Cazenave<sup>2</sup>, Marc Luetscher<sup>3</sup>, Christoph Spötl<sup>4</sup>,  
4 Fernando Gázquez<sup>5,6</sup>, Ánchel Belmonte<sup>7</sup>, Alexandra V. Turchyn<sup>8</sup>, Juan Ignacio  
5 López-Moreno<sup>1</sup>, Ana Moreno<sup>1</sup>

6 1 Departamento de Procesos Geoambientales y Cambio Global, Instituto  
7 Pirenaico de Ecología-CSIC, Zaragoza, Spain.

8 2 Société de Spéléologie et de Préhistoire des Pyrénées Occidentales  
9 (SSPPO), 5 allée du Grand Tour, 64000 PAU, France

10 3 Swiss Institute for Speleology and Karst Studies (SISKA), La Chaux-de-  
11 Fonds, Switzerland

12

13 4 Institute of Geology, University of Innsbruck, 6020 Innsbruck, Austria

14 5 Water Resources and Environmental Geology Research Group, Department  
15 of Biology and Geology, University of Almería, Almería, Spain.

16

17 6 Andalusian Centre for the Monitoring and Assessment of Global Change  
18 (CAESCG), University of Almería, Almería, Spain.

19

20 7 Sobrarbe-Pirineos UNESCO Global Geopark. Boltaña. Spain.

21 8 Godwin Laboratory for Palaeoclimate Research, Department of Earth Sciences,  
22 University of Cambridge, Cambridge, UK

23

24 \*Correspondence: Miguel Bartolomé (mbart@ipe.csic.es)

25

26 **Abstract**

27 Ice caves are one of the least studied parts of the cryosphere, particularly those  
28 located in inaccessible permafrost areas at high altitudes or high latitudes. We  
29 characterize the climate dynamics and the geomorphological features of Devaux  
30 cave, an outstanding ice cave in the Central Pyrenees on the French-Spanish  
31 border. Two distinct cave sectors were identified based on air temperature and

32 geomorphological observations. The first one comprises well-ventilated galleries  
33 with large temperature oscillations likely influenced by a cave river. The second  
34 sector corresponds to more isolated chambers, where air and rock temperatures  
35 stay below 0°C throughout the year. Seasonal layered ice and hoarfrost occupy  
36 the first sector, while transparent, massive perennial ice is present in the isolated  
37 chambers. Cryogenic calcite and gypsum are mainly present within the perennial  
38 ice. During winter, the cave river freezes at the outlet, resulting in a damming and  
39 back-flooding of the cave. We suggest that relict ice formations record past  
40 damming events with subsequent formation of congelation ice.  $\delta^{34}\text{S}$  values of  
41 gypsum indicate that the sulfate originated from the oxidation of pyrite present in  
42 the bedrock. Several features including air and rock temperatures, the absence  
43 of drips, the small loss of ice in the past seven decades, and the location of ice  
44 bodies in the cave indicate that the cave permafrost is the result of a combination  
45 of undercooling by ventilation and diffusive heat transfer from the surrounding  
46 permafrost, reaching a thickness of ~200 m.

47 **Keywords:** Ice cave, cave monitoring, cryogenic cave carbonates, cryogenic  
48 gypsum, Pyrenees.

## 49 1. Introduction

50 Mountain areas are among those environments most affected by current climate  
51 change (Hock et al., 2019). In the mid-latitudes, high-altitude areas are subject to  
52 mountain permafrost, a very sensitive and unstable phenomenon that responds  
53 quickly to environmental changes (Harris et al., 2003; Biskaborn et al., 2019) due  
54 to the number of factors. Snow cover distribution and thickness, topography,  
55 water availability, and surface and rock temperature influence the spatial  
56 distribution of mountain permafrost (Gruber and Haeberli, 2009). In light of these  
57 processes, multidisciplinary studies including, among others, measurements of  
58 rock temperature in boreholes and bottom temperatures of snow cover (BTS),  
59 geophysical techniques, and detailed mapping (geomorphology, thermal) are  
60 needed to gain a comprehensive understanding of mountain permafrost (e.g.  
61 Lewkowicz and Ednie, 2004; Serrano et al., 2019; Biskaborn et al., 2019). On the  
62 other hand, integrated studies of paleo-permafrost (e.g. Vaks et al., 2020) and  
63 modern permafrost, specifically mountain permafrost (e.g., Supper et al., 2014;

64 Scandroglio et al., 2021), shed light on past, present and future developments of  
65 permafrost areas, an issue of vital importance in the context of global warming.  
66 Studies of past permafrost require sedimentary records, which are locally  
67 preserved in caves located at high altitudes and/or high latitudes. Temporal and  
68 spatial changes in past permafrost distribution have been identified using  
69 speleothems (stalagmites, flowstones) in high-latitude and polar regions (e.g.,  
70 Vaks et al., 2013, 2020; Moseley et al., 2021; Li et al., 2021) as well as in mid-  
71 latitude regions (e.g., Lundberg and McFarlane, 2007; Fankhauser et al., 2016;  
72 Lechleitner et al., 2020).

73 Ice caves are cavities in rock hosting perennial ice that results from the  
74 transformation of snow and/or the freezing of infiltrating water (Perşoiu and  
75 Lauritzen, 2018). Cave ice can be dated and used as a valuable paleoclimate  
76 archive in non-polar areas (e.g., Stoffel et al., 2009; Spötl et al., 2013; Perşoiu et  
77 al., 2017; Kern et al., 2018; Sancho et al., 2018a; Leunda et al., 2019; Munroe,  
78 2021; Racine et al., 2022). Recently, coarse cryogenic cave carbonates  
79 ( $\text{CCC}_{\text{coarse}}$ ), that form during slow freezing of water inside caves, have been used  
80 as indicator of permafrost degradation, permafrost thickness, and subsurface ice  
81 formation (Žák et al., 2004, 2012; Richter et al., 2010a; Luetscher et al., 2013;  
82 Orvošová et al., 2014; Spötl and Cheng, 2014; Bartolomé et al., 2015;  
83 Dublyansky et al., 2018; Koltai et al., 2020; Munroe et al., 2021; Spötl et al.,  
84 2021).

85 Many ice caves are located in areas where the mean annual air temperature  
86 (MAAT) outside the cave is above  $0^{\circ}\text{C}$  (Perşoiu and Lauritzen, 2018) and,  
87 therefore, are highly susceptible to future climate warming (Kern and Perşoiu,  
88 2013). These ice caves are local thermal anomalies which are controlled by the  
89 cave geometry and the associated ventilation pattern. Their ice deposits  
90 represent sporadic permafrost occurrences and do not inform about the wider  
91 thermal environment. In contrast, at high altitudes and high latitudes subsurface  
92 ice deposits are still preserved by the presence of permafrost under the current  
93 climate conditions. There, mountain permafrost is limited to areas where a  
94 periglacial belt is present, with  $\text{MAAT} \leq 0^{\circ}\text{C}$ . For example, in the European Alps,  
95 discontinuous mountain permafrost is observed above 2600 to 3000 m a.s.l.  
96 (Boeckli et al., 2012), while in southern Europe permafrost is generally absent

97 (i.e. not observed even on the highest massif of the Iberian Peninsula, Gómez-  
98 Ortiz et al., 2019). In the Central Pyrenees few studies suggest the possible  
99 presence of permafrost above 2750 m a.s.l. (Serrano et al., 2019, 2020; Rico et  
100 al., 2021), and the presence of a few ice caves has only recently been  
101 documented (e.g. Sancho et al., 2018a; Serrano et al., 2018) informing about the  
102 occurrence of sporadic permafrost.

103 The aim of this study is to characterize the permafrost conditions in Devaux cave,  
104 a high-altitude ice cave in the Central Pyrenees. We monitored air, water and  
105 rock temperatures and used cryogenic cave deposits to i) document the  
106 distribution of permafrost within this cave, and ii) to study the processes that  
107 resulted in perennial cave ice bodies and associated cryogenic mineral  
108 occurrences.

109

## 110 **2. Study site**

111 Devaux cave opens at ~2838 m a.s.l. in the NE cliff of Gavarnie cirque (France)  
112 of the Monte Perdido massif (MPm) in the Central Pyrenees (Fig. 1a). The cave  
113 is located between the Parc National des Pyrénées (France) and the Parque  
114 Nacional de Ordesa y Monte Perdido (Spain). Named after Joseph Devaux who  
115 discovered and explored it in 1928, the cave was later investigated with respect  
116 to its hydrogeology and microclimatology and preliminary descriptions of its  
117 deposits were reported (e.g., Devaux, 1929; 1933; Rösch and Rösch, 1935;  
118 Rösch, 1949; du Cailar and Dubois, 1953; Requirand, 2014).

119

120 The area is dominated by limestones and dolostones ranging from the Upper  
121 Cretaceous to the Eocene-Paleocene. MPm is the highest limestone karst area  
122 in Europe reaching up to 3355 m a.s.l. (Monte Perdido peak) (Fig. 1b). The  
123 nearest peaks to Devaux cave are Marboré (3248 m a.s.l.) and the three Cascada  
124 peaks (3164 m, 3111 m, and 3098 m a.s.l.). The limestone thickness above the  
125 cave varies between ~200 and 250 m (Fig. 2a). In Devaux, the galleries follow  
126 the axis of a NW-SE striking syncline (Fig. 1b). A river runs along the cave (Fig.  
127 2a, b). The cave has two known entrances: the lower one corresponds to the  
128 main outlet of the cave river (Brulle spring, North 1, ~2821 m a.s.l.), while the

129 upper entrance is known as the “Porche” (South, ~2836 m a.s.l.) (Figs. 1c and  
130 2b). Between these two entrances, a small gallery (Spring North 2) opens +1.2 m  
131 above Brulle spring (Fig. 1c). Brulle is one of the main springs in the Gavarnie  
132 cirque. This spring drains a catchment of ~2.6 km<sup>2</sup> (polje) located on the southern  
133 face of MPm between ~2850 and 3355 m a.s.l. (Figs. 1b and, 1d). Major water  
134 flow is observed during late spring and early summer when snowmelt occurs in a  
135 catchment characterised by shafts, sinkholes and small closed depressions (Fig.  
136 1d). The water of Brulle spring feeds, together with some other springs located a  
137 few hundred meters below, the Gavarnie waterfall (Fig. 1b). A tracer experiment  
138 (du Cailar et al., 1953) indicated that part of the water of the Gavarnie waterfall,  
139 and thus likely also from Brulle spring, comes from a ponor in the Lago helado  
140 (lake, Fig. 1e) located ~2.3 km to the east of Devaux cave (Figs. 1b and 2a). The  
141 Gavarnie waterfall (Fig. 1b) turned green within ~21 hours after injection of the  
142 tracer but the water at Brulle spring was not directly checked (du Cailar et al.,  
143 1953). During the colder months, the spring as well as the Gavarnie waterfall  
144 freeze.

145 The geomorphology of the area is dominated by karst, glacial and periglacial  
146 landforms. The area was strongly glaciated during the last glacial period on both  
147 sides of the massif (e.g., Reille and Andrieu, 1995; Sancho et al., 2018b;  
148 Bartolomé et al., 2021). Today, only two glacier relicts covered by scree deposits  
149 are present in the Gavarnie cirque (Fig. 1b): 1) the Cascada dead-ice which is  
150 located several hundred meters below Devaux cave, and 2) a dead-ice  
151 accumulation in the NE wall of the cirque. Till present close to Brulle spring, on  
152 the access to Devaux and in the Cascada glacier, point to a much larger glacier  
153 extent in the past, maybe corresponding to the Little Ice Age or even the  
154 Neoglacial advance recognized in the nearby Tucarroya (Fig. 1b) and Troumouse  
155 cirques (Gellatly et al., 1992; González Trueba et al., 2008; García-Ruiz et al.,  
156 2014, 2020).

157 The study area lies at the transition between Atlantic and Mediterranean climate,  
158 with generally cold and dry winters and warm and dry summers. In MPm, the  
159 annual 0°C isotherm is located at ~ 2900 m a.s.l. (López-Moreno et al., 2016;  
160 Serrano et al., 2019). The wet seasons are fall and spring. The annual  
161 precipitation at the Góriz meteorological station (2150 m a.s.l. and 3 km SE of the

162 cave) averages 1650 mm. However, mass balance calculations of the nearby  
163 Monte Perdido glacier, where more than 3 m of snow (density 450 kg/m<sup>3</sup>)  
164 accumulates between November to April, indicates a minimum amount of 1500  
165 mm water equivalent, therefore the total annual precipitation in high parts of the  
166 massif exceeds 2500 mm (López-Moreno et al., 2019). In the MPm,  
167 discontinuous permafrost is present between ~2750 and ~2900 m a.s.l. and  
168 becomes more frequent above ~2900 m a.s.l. on the northern side (Serrano et  
169 al., 2019). Periglacial activity is characterized by rock glaciers, solifluction lobes  
170 and patterned ground (Feuillet, 2011).

171

### 172 **3. Material and methods**

#### 173 **3.1 Cave survey and mapping**

174 A survey of Devaux cave was conducted using a compass and clinometer as well  
175 as a laser distometer (Disto-X, Heeb, 2014). In addition to cave ice, chemical and  
176 clastic deposits were mapped in the cave (Fig. 2b). The labelling of the cave  
177 chambers (A to K) follows the nomenclature introduced by Devaux (1929) and  
178 Rösch and Rösch (1935).

179 A map of potential solar radiation (RAD) of the MPm was obtained using an  
180 algorithm which considers the effects of the surrounding topography on  
181 shadowing considering the position of the sun. RAD was calculated for every  
182 month and was then averaged to obtain an annual mean. Details of this  
183 computation can be found in Pons and Ninyerola (2008).

#### 184 **3.2 Cave monitoring**

185 The cave consists of large rooms (e.g., room F, and those located beyond SCAL  
186 chatière) connected by small galleries (Fig. 2b), locally with narrow passages  
187 (e.g., galleries close to SPD room or SCAL chatière, Fig. 2b). 15 stations were  
188 installed in the outmost ~350 m of the cave to monitor air (11 sensors), water (2  
189 sensors) and rock temperature (2 sensors) (Fig. 2b). Cave air temperature  
190 variations were recorded using different devices (Hobo Pro v2 U23-001 (accuracy  
191 ±0.25°C, resolution 0.02°C), Tinytag Talk 2 (accuracy ±0.5°C, resolution, 0.04°C)  
192 and ELUSB2 (accuracy ±0.21°C, resolution 0.5°C)). The cave river temperature

193 was recorded at two points. The first site (W7) was located close to the Brulle  
194 spring (Fig. 2b; Hobo TiDBit V2, accuracy  $\pm 0.21^{\circ}\text{C}$ , resolution  $0.02^{\circ}\text{C}$ ) and, the  
195 second site (W6) was located in room F (Fig. 2b; Hobo UA-001-08; accuracy  
196  $\pm 0.53^{\circ}\text{C}$ , resolution  $0.4^{\circ}\text{C}$ ). Both sensors were installed at a water depth of 20  
197 cm. Finally, the rock temperature was recorded at two sites (R1 and R2 in room  
198 D and K, respectively) using a Hobo U23-003 device (accuracy  $\pm 0.25^{\circ}\text{C}$ ,  
199 resolution  $0.02^{\circ}\text{C}$ ). Each sensor has two external temperature probes (channels  
200 1 and 2, Ch1-Ch2). These temperature probes were installed in two horizontal  
201 drill holes of 60 cm depth,  $\sim 1.5$  to 2 m from each other.

202 We monitored sporadically the cave during different intervals between 2011 and  
203 2015, while a continuous monitoring was carried out between July 2017 and July  
204 2021. Maximum, minimum and mean temperatures as well as the number of  
205 frost/warm days were obtained for each sensor and site (Fig. 2b). Changes in the  
206 ice morphology were evaluated using wall marks measured at four points since  
207 2013 in room G and using one point during 2020-2021 in room SPD (Fig. 2b)  
208 using a digital sliding caliper.

209 The outside temperature was measured at the “Porche” entrance ( $\sim 2836$  m a.s.l.)  
210 and on the southern face of MPM at  $\sim 2690$  m a.s.l. For comparison, these  
211 temperature records were corrected assuming an adiabatic lapse rate of  $5.5^{\circ}\text{C}$   
212  $\text{km}^{-1}$  (López-Moreno et al., 2016; Navarro-Serrano et al., 2018) to an elevation of  
213  $\sim 2850$  m a.s.l., corresponding approximately to the lower limit of the hydrological  
214 catchment area of Devaux. In both cases, the temperature was measured using  
215 Tinytag Talk 2 sensors equipped with a radiation shield. These data were  
216 compared to the temperature record from the Pic du Midi de Bigorre  
217 meteorological station (PMBS; 2011-2020) (2860 m a.s.l.,  $\sim 28$  km N of Devaux)  
218 obtained from Météo-France. Moreover, the homogenised data available since  
219 1882 from PMBS (Bücher and Dessens, 1991; Dessens and Bücher, 1995) were  
220 used to identify long-term temperature trends.

### 221 **3.3 X-ray diffraction, ion chromatography and sulfur isotopes**

222 X-ray diffraction (XRD) analyses were performed on sulfate and carbonate  
223 crystals from rooms G, D and K, as well as on sulphide and oxidized crystals  
224 thereof from the host rock (Fig. S1). The analyses were performed at the

225 Geosciences Institute in Barcelona (GEO3-BCN-CSIC) using a Bruker-AXS  
226 D5005 powder diffractometer configured in  $\theta/2\theta$ -mode (e.g. Rodríguez-Salgado  
227 et al., 2021).

228 Samples of cave drip water, ice and river water were analysed for major ions by  
229 ion chromatography (IC) at the laboratories of the Pyrenean Institute of Ecology  
230 (Zaragoza). Carbonate alkalinity was determined by titration within 24 hours after  
231 sampling.

232 Sixteen samples, including sulfate crystals, dissolved sulfate and pyrite crystals  
233 were selected for sulfur isotope analysis at the Godwin Laboratory for  
234 Paleoclimate Research of the University of Cambridge (UK), following the  
235 methodology of Giesemann et al., (1994). For gypsum samples, ~5 mg of  
236 powdered gypsum were dissolved in deionized water at 45°C overnight. Then, a  
237 BaCl<sub>2</sub> solution (50 g/L) was added to induce BaSO<sub>4</sub> precipitation. In the case of  
238 water samples, BaCl<sub>2</sub> was added directly to the sample. Subsequently, 6M HCl  
239 was added to remove any co-precipitated carbonate minerals and the BaSO<sub>4</sub>  
240 precipitate was rinsed several times with deionized water. Finally, BaSO<sub>4</sub> was  
241 dried at 45°C overnight. Sulfate dissolved in water were precipitated using the  
242 same method.

243 Isotope measurements were carried out using a Flash Elemental Analyzer (Flash-  
244 EA) at 1030 °C. The samples were folded in tin capsules. After sample  
245 combustion, the generated SO<sub>2</sub> was measured by continuous-flow gas source  
246 isotope ratio mass spectrometry (Thermo Scientific, Delta V Plus). Samples were  
247 run in duplicate and calibration was accomplished using NBS-127. The  
248 reproducibility ( $1\sigma$ ) of  $\delta^{34}\text{S}$  was better than 0.2‰, similar to the long-term  
249 reproducibility of the standard over the run (0.2‰).  $\delta^{34}\text{S}$  isotope values are  
250 reported relative to VCDT (Vienna-Canyon Diablo Troilite).

251

## 252 **4. Results**

### 253 **4.1 Devaux cave description**

254 Devaux cave is ~2500 m long and comprises three distinct levels (Fig. 2b). The  
255 lower and the middle levels correspond to the Brulle spring (0 m), and the  
256 “Porche” entrance (~+14.5 m), respectively. The third one comprises chambers



257 and galleries +21 m to +29 m above the Brulle spring (Fig. 2b). In the inner part  
258 of the cave, some unexplored vertical chimneys may connect to sinkholes in the  
259 catchment above the cave (Fig. 2a). The main ice deposits are located in rooms  
260 D, G, SPD and K (Fig. 2b). Except for SPD, these chambers located above the  
261 Porche entrance (between ~+1 and +7 m) can be accessed via ascending  
262 passages.

263 During the cold season, the cave river starts freezing at the spring and the ice  
264 then expands backward into room F (Fig. 2b). The ice totally or partially clogs the  
265 main gallery and dams the water inside the cave forming a small lake (cf. also  
266 Rösch and Rösch, 1935). This process is important for the seasonal ice extent  
267 as the flooding of the cave depends on whether the springs (North 1 and North  
268 2) are frozen or not (e.g., Rösch and Rösch, 1935). Webcam observations  
269 (Gavarnie, Oxygène hut) suggest a possible freezing of the Brulle spring from  
270 late November to mid-May simultaneous with the freezing of the Gavarnie  
271 waterfall. Moreover, historical photos (e.g., Devaux, 1929; Rösch and Rösch,  
272 1935) and our own observations show that snow during winter and spring can  
273 reach the Brulle entrance - a situation that also favours the blocking of the  
274 springs. As a result of such flooding events, slackwater deposits formed in the  
275 cave entrance zone, but locally also further into the cave (e.g., in rooms I, J, K  
276 and SCAL chatière, along the main gallery; Fig. 2b), while silty sediments are  
277 found at elevated positions with respect to the river level (e.g., in rooms D and  
278 G). Sandy sediments dominate in the large rooms located beyond the SCAL  
279 chatière. Two such successions (~1 m thick) comprising hundreds of rhythmic  
280 fine sand and silt layers are present in elevated areas with respect to the current  
281 river, witnessing major events of back-flooding.

282 Observations made during summer show a dominant air-flow direction from the  
283 inner to the outer parts of the cave, exiting through the Brulle and Porche  
284 entrances. Conversely, the opposite is expected for the cold season (chimney  
285 effect). When the Brulle spring is partially clogged by ice during early summer  
286 forcing the stream to flow below the ice, air flows from room F to C (Fig. 2b) (e.g.,  
287 summer 2021). The air flow is imperceptible in rooms D, G, and close to K located  
288 away from the main cave passages.

## 289 **4.2 Climate setting of Devaux cave**

290 The MAAT at the elevation of Devaux cave is  $\sim 0$  °C ( $-0.04$  °C; 2017-2021). On  
291 the other hand, a positive MAAT ( $1.8$  °C) is recorded on the southern side of the  
292 MPm at a similar altitude (Fig. 3a). Maximum and minimum air temperatures  
293 outside the cave vary between  $24.5$  °C and  $-17.2$  °C (hourly values, 2017-2021).  
294 The PMBS MAAT record (Fig. 3b) shows a warming trend of around  $+1.5$  °C since  
295 the beginning of the measurements in 1882. Before 1985, temperatures below  
296  $0$ °C dominated the annual cycle, while positive MAATs became more frequent in  
297 recent years. Minimum temperatures also show a increasing trend of  $\sim +2.5$  °C,  
298 while the maximal annual temperatures do not show a clear trend. The north-  
299 facing Gavarnie cirque is associated with a clear RAD anomaly (Fig. 4). Values  
300 lower than  $215$  kWh/m<sup>2</sup> are observed at  $\sim 2000$  m and between  $\sim 2800$  and  $2900$   
301 m a.s.l., corresponding to the cirque bottom, the area located behind La Torre  
302 peak and the surroundings of Devaux cave. At the cave entrance the RAD value  
303 is only  $390$  kWh/m<sup>2</sup>, in stark contrast to the summit areas and surroundings where  
304 the RAD often exceeds  $1500$  kWh/m<sup>2</sup> (Fig. 4).

305 While the mean daily air temperature (MDAT) at the cave entrance (purple line in  
306 Fig. 5) and the temperature series from PMBS (pink line in Fig. 5) agree in their  
307 absolute values, the variability of MDAT at the Devaux entrance is lower than at  
308 the PMBS. This pattern could be related to local topographic conditions leading,  
309 for instance, to less RAD, or to the position of the sensor in the cliff (less night  
310 emissivity). Given this radiation contrast, warmer temperatures prevail on the  
311 southern side of the MPm (Fig. 4), favouring early snowmelt in spring and early  
312 summer, while at the same time the temperature stays below  $0$  °C in the cave's  
313 surroundings.

## 314 **4.3 Devaux cave temperature variations**

315 The cave can be separated into distinct areas depending on their thermal regime:  
316 ventilated galleries (rooms A, B, C, F and the main gallery from SPD to SCAL  
317 chatière)) and poorly ventilated parts off the main air flow path (rooms D, G, K -  
318 Figs. 2b, 5).

### 319 **4.3.1 Well-ventilated cave parts**

320 Air ( $T_{2\text{air}}$ ,  $T_{5\text{air}}$ ,  $T_{10\text{air}}$ ,  $T_{11\text{air}}$ ) and water ( $W_{6\text{water}}$ ,  $W_{7\text{water}}$ ) temperature data show  
321 large seasonal oscillations. All sensors except  $T_{11\text{air}}$  show a few days of positive  
322 temperatures during summer. Sensor  $T_{2\text{air}}$  (2011-2012, Fig.5a), which is also the  
323 closest to the Porche entrance, shows the highest correlation ( $r$ ) with the external  
324 temperature (0.73,  $p < 0.001$ ). Sensor  $T_{5\text{air}}$  (2017-2021, Fig. 5d) in room B also  
325 shows a high correlation and significant correlation (0.82,  $p < 0.0005$ ) with the  
326 outside temperature. During the major cave cooling that takes place between the  
327 end of October and May and the correlation is significant and ranges between  
328 0.68 to 0.84. During summer and part of fall, the correlation decreases notably (-  
329 0.23 to 0.76). Sensor  $T_{11\text{air}}$  (2018-2021, Fig. 5d) is partly protected from the air  
330 flow and shows lower a correlation (0.69,  $p < 0.001$ ) despite being located in a  
331 well-ventilated gallery (SPD room). Also during the winter months, the  
332 correlations are lower (0.49-0.62,  $p < 0.001$ ) than in  $T_{5\text{air}}$ . Sensor  $T_{10}$  (2014-  
333 2015, Fig. 5c) does not show any significant correlation with the external  
334 temperature.

335 Sensors  $W_{6\text{water}}$  and  $W_{7\text{water}}$  (Figs. 5b, c) recorded water temperature variations  
336 during the years 2012-2013 and 2014-2015, respectively. Both sensors record a  
337 continuous temperature decline from the end of November to mid-January until  
338 the water freezes. At  $W_{7\text{water}}$ , the temperature ranges between -0.3 and -5.8 °C  
339 between the end of fall and the beginning of winter, while the temperature stays  
340 close to 0°C between January and the beginning of June. At  $W_{6\text{water}}$ , the  
341 temperature reached a minimum of -1.7 °C and shows smaller variations than at  
342  $W_{7\text{water}}$ . No significant correlation was found between the external air temperature  
343 and the river water temperature. Only  $W_{6\text{water}}$  shows a weak correlation with the  
344 external temperature when ice is absent (0.39  $p < 0.001$  and 0.40  $p < 0.001$ ).

345 For each monitored interval, the mean annual cave temperature at the  $T_{2\text{air}}$ ,  $T_{5\text{air}}$   
346 and  $T_{11\text{air}}$  sensors is lower than the outside mean temperature (by 0.4°, 2.0°, 3.3°  
347 C, respectively). The  $W_{6\text{water}}$ ,  $W_{7\text{water}}$  and  $T_{10\text{air}}$  sensors show mean  
348 temperatures higher than the external mean temperatures (by 1.6°, 2.6°, 2.5° C,  
349 respectively). The periods 2011-2012 and 2017-2018 (at  $T_{2\text{air}}$  and  $T_{5\text{air}}$ ,  
350 respectively) represent the coldest cave years of the monitoring period.

351

352 **4.3.2 Poorly ventilated cave parts**

353 Sensors located in rooms D ( $T_{3\text{air}}$ ,  $T_{4\text{air}}$ ,  $T_{8\text{air}}$ ), G ( $T_{9\text{air}}$ ), K ( $T_{12\text{air}}$ ) and rock  
354 temperature ( $R_{1\text{rock}}$ ,  $R_{2\text{rock}}$ ) show air temperatures below 0 °C during the  
355 monitoring period with small oscillations and a weak and/or insignificant  
356 correlation with the external air temperature. Sensor  $R_{1\text{rock}}$  (Fig. 5) recorded rock  
357 temperatures consistently below 0°C during the entire monitoring period. This  
358 sensor shows constant rock temperatures (-1.24 °C and -1.27 °C for channels 1  
359 and 2, respectively), similar within error to the cave air temperature ( $T_{3\text{air}}$ ,  $T_{9\text{air}}$ ;  
360 2019-2021). All sensors except for  $T_{3\text{air}}$  (2011-2012, Fig. 5a) show mean air and  
361 rock temperatures lower than the mean external temperature during the same  
362 period (by 0.59 °C to 2.47°C). The muted temperature variations in these  
363 chambers reflect reduced heat exchange compared to the well-ventilated parts  
364 of the cave. Sensors  $T_{12\text{air}}$  and  $R_{2\text{rock}}$  are located in room K, and similar to  $T_{11\text{air}}$ ,  
365 the chamber morphology shields them from the air flow. Rock temperature sensor  
366  $R_{2\text{rock}}$  shows a slightly more variable temperature ranging between -0.19°C and  
367 -0.28°C (mean of -0.24 and -0.23°C for channel 1 and 2, respectively). Sensor  
368  $T_{12\text{air}}$  shows a low correlation with the external temperature ( $r^2=0.35$ ,  $p<0.001$   
369 (2018-2021)), and the same is observed for  $T_{\text{ext}} - R_{2\text{rock}}$  ( $r^2=0.35$ ,  $p<0.001$  (2019-  
370 2021). Meanwhile the correlation between  $T_{12\text{air}}$  and  $R_{2\text{rock}}$  is high but not  
371 significant ( $r^2=0.93$ ,  $p>0.005$  (2019-2021)).

372

373

374 **4.4 Cave deposits**

375 **4.4.1 Ice**

376 Congelation ice formed by freezing of water within the cave is the most abundant  
377 type of ice, and four main ice deposits are located in chambers D, G, SPD, and  
378 K (Fig. 2b). The most relevant feature of these ice bodies is their high  
379 transparency and massive aspect, i.e. the lack of layering (Figs. 6a, b).  
380 Transparent ice is present on the ceiling, blocking chimneys, galleries and  
381 fractures. The local loss of transparency is related to the presence of cryogenic  
382 cave minerals and/or air inclusions (Figs. 6a, b, c, d).

383 A highly transparent ice deposit covers the southwest wall of room D and blocks  
384 the access to a gallery (Fig. 6a). The height of this deposit reaches ~6 m, and its  
385 base is located ~20 m above the Brulle spring. The thickness of this ice deposit  
386 ranges from 4.5 to 14.5 m (horizontal laser measurements across the ice in the  
387 gallery blocked by ice) and the estimated volume ranges from ~350 to ~710 m<sup>3</sup>.  
388 Three unconformities marked by cryogenic minerals were identified in this ice  
389 body.

390 In room G, an ice body (~25.8 to 29.6 m above the Brulle spring) is present on  
391 the ceiling (Fig. 6b) and the estimated ice volume is ~180 m<sup>3</sup>. A comparison with  
392 a historical photograph shortly before 1953 (Casteret, 1953) suggests that the ice  
393 body has not changed significantly during the last ~69 years (Figs. 7a, b). Ice-  
394 rock distances measured at four points, however, reveal small changes at three  
395 of them. The first has retreated 9.8 mm since 2014 (mean 0.9 mm a<sup>-1</sup>, n=2), the  
396 second has retreated 19.2 mm since 2014 (mean 0.6 mm a<sup>-1</sup>, n=5), and the third  
397 one has retreated 15.8 mm since 2013 (mean 2.2 mm a<sup>-1</sup>, n=7). At ~80 m from  
398 the entrance, a small descending room (SPD) (Figs. 2b, 6c) hosts a small volume  
399 of ice. Measurements between 2020 and 2021 indicate a retreat of 20 mm a<sup>-1</sup>  
400 (n=1). A last major ice deposit is present ~280 m from the entrance (room K),  
401 where transparent and massive ice (~15.5 m above the Brulle spring) currently  
402 fills a cupula or chimney (Figs. 2b, 6d). Additional ice bodies are present behind  
403 the SCAL chatière in the upper gallery (Fig. 2b), but they have not been studied.

404 In contrast to these massive ice deposits, layered ice of seasonal origin is present  
405 in small chambers adjacent to the river (E and F rooms) (Fig. 6e). This ice forms  
406 sheets of about 10-15 cm in thickness which are present in room F and nearby  
407 areas (Fig. 6f). This ice is related to the damming and freezing of water inside the  
408 cave when the Brulle spring freezes. Our visits from 2017 to 2021 revealed that  
409 most of the damming and subsequent ice formation in room F took place during  
410 winter and spring 2017-2018 corresponding with the coldest months (both inside  
411 the cave and outside) of the monitoring period (Fig. 5d). These ice slabs are  
412 characterized by flat surfaces on both sides and obviously record incomplete  
413 freezing of the dammed water. The ice sheets largely disappeared during  
414 summer and fall, and only strongly degraded ice remained in elevated areas of  
415 room F.

416 On the other hand, ice sheets associated with earlier episodes of river damming  
417 and freezing have disappeared, and only linear colour changes remained as  
418 witnesses of such events on the walls of the room E (Fig. 8d). A historical  
419 photograph exemplifies these ice levels in the access between rooms F and E  
420 (Fig. 8a). In August 1984 the ice was close to the ceiling and nearly 1 m thick  
421 (Fig. 8a; Marc Galy, pers. comm.). This contrasts with the low ice level in recent  
422 years (Fig. 8b). In total, three ice-level marks were identified in relation to back-  
423 flooding and subsequent freezing of ponded water (Figs. 8c, d). They appear at  
424 a lower elevation than the Porche entrance (c.+9.5, +9.2, +8.8, m with respect to  
425 the Brulle spring).

426 Another important feature is the presence of hoarfrost, which was observed in  
427 rooms A, B,C, E, F and along the gallery between SPD and J (Figs. 2b, 7g, h).  
428 The crystal size varies from few mm to 4 cm and appears to be upholstering some  
429 galleries and cupolas, forming aggregates that hang from the ceiling (Fig. 6h).  
430 Finally, seasonal ice formations (e.g., icicles and ice stalagmites), as well as drips  
431 are restricted to the outmost ~15 m, in the vicinity of both entrances, and in the  
432 innermost part of the cave (~ 500 m from the entrance). Seasonal ice formations  
433 are absent in cave sectors where transparent ice bodies and hoarfrost are  
434 present. Firn deposits derived from snow are restricted to the Porche entrance.

435

#### 436 **4.4.2 Mineral deposits**

437 They comprise mainly cryogenic cave minerals. XRD analyses of samples from  
438 rooms D, G and K yielded gypsum and calcite, while the sulfide crystals and their  
439 oxidation products present in the host rock were identified as pyrite and goethite,  
440 respectively. The presence of cryogenic gypsum in Devaux was already reported  
441 by du Cailar and Dubois (1953). In room D, gypsum was observed within the ice  
442 and on boulders (Figs. 9a, b, c). A total of three gypsum levels (lower, middle and  
443 upper, located at ~21.4, ~22.6 and ~23.9 m, respectively, with respect to the  
444 Brulle spring) were identified in the ice (Fig. 9a). Due to the progressive retreat of  
445 the ice body, some of these crystals are now present on the ice surface. Gypsum  
446 levels comprise large single crystals (0.5-1 cm in diameter), aggregates forming  
447 rafts (10 cm) up to 1 cm in thickness (Fig. 9b), as well as a fine crystalline fraction.

448 Examination of the fine fraction using a binocular stereo microscope indicates the  
449 presence of cryogenic cave carbonates and gypsum (CCG) including globular,  
450 single and twin morphologies <1 mm in diameter (Fig. 9d).

451

452 In room G, gypsum and carbonates crystals are present in the lower part of the  
453 ice deposit (Fig. 10e) and on blocks. There, CCC are larger (>10 mm) than in  
454 room D and include globular shapes and raft-like aggregates, similar to those  
455 reported by Žák et al. (2012). Some of these CCC show gypsum overgrowths  
456 (Fig. 9f). Across the ice surface, patches of globular CCC (sub-millimetre size)  
457 have been released by ice sublimation (Figs. 7a, b). In room SPD, CCC and CCG  
458 ( $\leq 2$  mm) are present within and on the ice (Figs. 2b, 7c). Finally, in room K, only  
459 few CCC were still present within the ice, while most of them form heaps of loose  
460 crystals covering blocks. Some of these CCC exceed 5 mm in diameter. Crystal  
461 morphologies include rosettes, skeletons and rhombohedrons similar to those  
462 reported by Žák et al. (2012) as well as white tapered crystal aggregates. Beyond  
463 room K, regular carbonate speleothems (i.e. stalagmites, stalactites and  
464 flowstones) are present. Gypsum coating walls or ceilings was not observed.

#### 465 **4.5 Cave water chemistry and sulfate isotopic composition**

466 The chemical composition of water in Devaux cave is dominated by calcium and  
467 bicarbonate with relatively high Mg concentrations and locally also elevated  
468 sulfate concentrations (Table 1). Total dissolved solids (TDS, n=7) vary from 57  
469 to 315 mg l<sup>-1</sup>. Devaux's dripwater has higher mean sulfate concentrations (65 mg  
470 l<sup>-1</sup>) than the cave river (11 mg l<sup>-1</sup>) and massive and seasonal ice (2.8-18 mg l<sup>-1</sup>).  
471 The  $\delta^{34}\text{S}$  value of dissolved sulfate in the dripwater is -14.4‰ (n=1), which is  
472 significantly higher than in cave river water (-28.5‰ to -27.3‰, n=2; Table 2).  
473 Gypsum crystals in room D show  $\delta^{34}\text{S}$  values ranging from -15.1‰ to -15.8‰  
474 (n=7), while in room G they range from -12.3‰ to -11.9‰ (n=5). A pyrite sample  
475 from the host rock yielded a  $\delta^{34}\text{S}$  value of -12.7‰ (n=1).

## 476 **5. Discussion**

### 477 **5.1. Processes controlling the thermal regime in Devaux cave and the extent of** 478 **permafrost**

479 A complex spatial distribution and a high degree of heterogeneity are among the  
480 main characteristics of mountain permafrost (Gruber and Haeberli, 2009). In  
481 Devaux cave the existence of permafrost can be related to a combination of two  
482 processes: i) cave atmospheric dynamics, and ii) conductive heat transfer  
483 through the rock.

484 Devaux cave is characterized by mean air and rock temperatures lower than the  
485 external mean annual temperature (Fig. 5). The low cave temperatures in winter  
486 lead to an inward airflow and an associated negative thermal anomaly behind the  
487 entrance zone. On the contrary, during summer the cold and dense air flows out  
488 of the cave due to the temperature difference between outside and inside air. The  
489 heat supplied to the cave by the river also influences the cave air temperature by  
490 exporting thermal energy from the cave during winter. Similar seasonal ventilation  
491 patterns have been observed in ice caves elsewhere (e.g., Luetscher et al., 2008;  
492 Colucci and Guglielmin, 2019; Perşoiu et al., 2021).

493 On the other hand, positive temperatures are observed both in the cave river and  
494 in the air at the entrance (Fig. 5), reflecting heat advected by water (river) and the  
495 influence of the external temperature (cf. Luetscher et al., 2008; Badino, 2010).  
496 The lack of correlation between the external and internal temperatures and the  
497 small temperature variability in rooms D, G, and K reflect their thermal isolation  
498 from well-ventilated cave parts. There, the apparent thermal equilibrium between  
499 the rock and the cave atmosphere ( $T_{\text{rock}}=T_{\text{air}}$ ) supports the notion that heat  
500 exchange is dominated by conduction through the bedrock.

501 The MAAT at the altitude of the cave is  $-0.04\text{ }^{\circ}\text{C}$  (2017-2021) suggesting that the  
502  $0\text{ }^{\circ}\text{C}$  isotherm is located close to the cave. Using an array of techniques (geomatic  
503 surveys, temperature monitoring, temperature at the base of the snowpack (BTS)  
504 and geomorphological and thermal mapping), Serrano et al. (2019) observed  
505 mean annual ground temperatures between  $-1$  and  $-2\text{ }^{\circ}\text{C}$  on the northern slope  
506 of the MPm suggesting that discontinuous permafrost is present between 2750-  
507 2900 m a.s.l., with more continuous permafrost starting at 2900 m a.s.l. The  
508 orientation of the Gavarnie cirque, as well as the high slope angle, and shadow  
509 from the surrounding peaks favour the preservation of permafrost at lower  
510 elevations (e.g., Gubler et al., 2011).



511 Given the high thermal inertia of the rock, the permafrost temperature at depth is  
512 still under the influence of past climate conditions (e.g., Haeberli et al., 1984;  
513 Noetzli and Gruber, 2009) and, therefore, part of the current permafrost in the  
514 area could be inherited from previous colder times (e.g., Colucci and Guglielmin,  
515 2019). In particular, the low mean annual temperatures recorded at PMBS in the  
516 late 19<sup>th</sup> century were favourable conditions for permafrost development. We  
517 surmise that the current permafrost could be inherited from colder periods of the  
518 Little Ice Age.

519 In well-ventilated ice caves hoarfrost is the most dynamic ice formation on  
520 seasonal time scales. The presence of perennial hoarfrost is, however, indicative  
521 of a continuously frozen bedrock and thus representative of caves within the  
522 permafrost zone (e.g. Luetscher and Jeannin, 2018; Yonge et al., 2018). In  
523 Devaux cave, perennial hoarfrost is observed in rooms where the bedrock is  
524 surrounded by small ice bodies (e.g., gallery close to SPD room, Fig. 6g). Devaux  
525 (1929) indicated the presence of ice crystals on the ceiling at the entrance of  
526 room D. In the same way, du Cailar and Dubois (1953) showed a schematic  
527 cross-section of room D, where ice crystals are present at the beginning of the  
528 room. These historical reports suggest these areas were probably more  
529 ventilated in the past, which favoured the hoarfrost formation. On the other hand,  
530 seasonal hoarfrost is present in ventilated galleries (A, B, C, F and between SPD  
531 and J). Seasonal hoarfrost in room B and C, and in the area between H to J,  
532 disappears at the end of summer, probably because of the heat delivered by the  
533 cave river, as recorded by the T5 sensor (Fig. 5).

534 The presence of permafrost in Devaux's catchment is supported by the absence  
535 of drips and/or seepage in the investigated cave passages (e.g., Luetscher and  
536 Jeannin, 2018; Vaks et al., 2020). Active drips and seasonal ice formations are  
537 limited to the first ~15 m of the cave as well as to the inner part (beyond room K).  
538 Mountain permafrost thus penetrates ~350 m longitudinally from the eastern cliff  
539 of the Gavarnie cirque to the southern side of the massif. On the other hand,  
540 given the elevation of the cave and the topography above the cave, the current  
541 maximum permafrost thickness on the southern side of the MPm is ~200 m  
542 (without taking into account the active layer).

543

## 544 **5.2. The origin of ice in Devaux cave**

545 The transparent and massive character of Devaux's cave ice, as well as the  
546 presence of CCC, which formation requires low congelation rates (Žák et al.,  
547 (2004)), suggests that this ice formed by slow freezing of water dammed by ice  
548 at the spring. This model is consistent with the climate of the Gavarnie cirque,  
549 cave geomorphological observations, cave air and water temperatures as well as  
550 historical reports. The cave water level can rise by several meters as indicated  
551 by slackwater deposits upstream of the Brulle spring.

552

553 The distribution and characteristics of ice bodies in Devaux cave indicate that the  
554 hydraulic head rose by at least ~ 15 - 29 m, which is the elevation of the ice bodies  
555 in rooms G, F and K. This situation requires that all springs (including Porche)  
556 are blocked for a sufficiently long time to allow for complete freezing of these cave  
557 lakes. The lack of important unconformities in this massive ice (e.g., detrital  
558 layers), which are usually related to seasonal ablation (e.g., Luetscher et al.,  
559 2007; Stoffel et al., 2009; Hercman et al., 2010; Spötl et al., 2013), suggests that  
560 the ice deposit in room G it is the result of a single flood event. On the contrary,  
561 the small unconformities recognized in the ice body in room D suggest that  
562 several cycles of damming and subsequent ice formation cannot be discarded in  
563 the formation of this ice deposit.

564

565 These observations indicate that under the current climate (both in the cave and  
566 outside) only part of the water dammed in rooms F and E freezes during winter  
567 and spring. This strongly suggests that the ice bodies in Devaux cave must have  
568 been associated with colder and/or longer events of ponding and freezing than  
569 today, when the cave was effectively sealed from the outside for prolonged times.  
570 We hypothesize that the advance of a glacier on the steep slopes of Devaux's  
571 surroundings could have contributed to the blockage of the spring, leading to  
572 backflooding and the formation of large ice bodies in the cave. In the study area,  
573 such periods of glacier growth occurred during the Little Ice Age and/or the  
574 Neoglacial (González Trueba et al., 2008; García-Ruiz et al., 2014, 2020).

575

576 The freezing of a flooded cave passage cannot be explained by the advection of  
577 cold air alone. It is thus surmised that heat transfer through the host rock is a  
578 more plausible mechanism for the complete freezing of ponded water. The cave  
579 ice bodies as well as the presence of cryogenic minerals therefore record a long  
580 cold period or several shorter episodes. Although cryogenic minerals and in  
581 particular CCC<sub>coarse</sub> are typically associated with permafrost thawing during warm  
582 spells (Žák et al., 2004; Richter et al., 2010; Žák et al., 2012; Luetscher et al.,  
583 2013), permafrost conditions prevailed during ice formation in Devaux cave. The  
584 water that feeds Devaux's springs infiltrated during late spring and summer from  
585 ponors at Lago helado and/or surrounding poljes. However, the heat supplied by  
586 this water may have probably not been enough to thaw the frozen host rock. It is  
587 thus very likely that the hostrock temperature was lower and/or the outlets  
588 remained closed for longer periods than today to allow for the complete slow  
589 freezing of the ponded water.

590

### 591 **5.2.1 Ice volume changes**

592 The colour changes in the walls close to the river (room E), the historical  
593 photograph as well as speleological reports point to large changes (several  
594 meters) in the height of the seasonal ice in the flood-prone sector of the cave  
595 (Figs. 8a, b). This ice is influenced by the heat exchanged between the water and  
596 the cave.

597 In contrast, changes in the ice volume are almost negligible in rooms D and G  
598 where the temperature is more constant and below 0°C (Figs. 7a, b). The ice  
599 body in room G has been retreating by only ~0.6 to ~2.2 mm a<sup>-1</sup>. A similar value  
600 (3 mm a<sup>-1</sup>) was observed in Coulthard cave (Alberta, British Columbia, Marshall  
601 and Brown, 1974), a cave located in permafrost (Yonge et al., 2018). Changes in  
602 the ice body in this cave were related to slow sublimation due to convective air  
603 flow inside the cave (Marshall and Brown, 1974). On the other hand, the ice in  
604 SPD room shows higher ice retreat rates (~ 20 mm a<sup>-1</sup>). Similar sublimation rates  
605 have been reported in 'ice caves in the Pamir Mountains and the northern part of  
606 the Russian Platform (Mavlyudov, 2008; Žák et al., 2018). Overall, Devaux's cave  
607 ice deposits show a remarkable stability which contrasts with the rapid changes

608 observed in ice caves outside permafrost areas (Kern and Perşoiu, 2013; Perşoiu  
609 et al., 2021; Wind et al., 2022), including other ice caves in the Pyrenees and  
610 Picos de Europa (Belmonte-Ribas et al., 2014; Gomez-Lende et al., 2014, 2016).

611

### 612 **5.3. Cryogenic cave minerals**

613 In Devaux cave, CCC and CCG are still present within the ice (Figs. 6, a, b, c, d).  
614 Worldwide, only very few *in situ* observations of coarse-grained cryogenic cave  
615 minerals are known (e.g., Bartolomé et al., 2015; Colucci et al., 2017). du Cailar  
616 and Dubois (1953) reported the presence of gypsum crystals at ~50 cm depth  
617 within the ice in Devaux cave. The first evidence of *in situ* CCC<sub>coarse</sub> in cave ice  
618 was reported from Sarrios 6, an ice cave at 2780 m a.s.l. on the southern slope  
619 of the MPm (Bartolomé et al., 2015). Colucci et al. (2017) documented the  
620 presence of CCC<sub>coarse</sub> in a small ice cave in the Italian Alps. Recently, Munroe et  
621 al. (2021) found CCC<sub>coarse</sub> in ice of Winter Wonderland cave (Utah, USA).  
622 Because of the abundance of cryogenic cave minerals, the size of individual  
623 crystals and aggregates thereof, and their different mineralogy, Devaux cave  
624 provides an additional opportunity for studying the origin of such cryogenic cave  
625 minerals.

626

627 CCG in Devaux cave represents, to our knowledge, the first occurrence of its kind  
628 in a carbonate karst terrain. So far, CCG have only been reported from gypsum  
629 karst areas in Russia and Ukraine (Korshunov and Shavrina, 1998; Žák et al.,  
630 2018 and references therein). In those caves, tiny gypsum crystals form during  
631 rapid freezing of water. When ice sublimates in winter, these particles are  
632 released and accumulate as powdery deposits on the ice surface. Eventually,  
633 they partly dissolve during spring and summer due to the increase in cave air  
634 humidity, and later recrystallize forming a wide variety of crystal morphologies.  
635 CCG from Devaux cave shows features that do not correspond to those  
636 previously published from gypsum karst caves. In particular, the Devaux cave  
637 CCG i) appears together with CCC<sub>coarse</sub> crystals ( $\geq 5$  mm in some cases, in rooms  
638 D and G), ii) the (raft-like) gypsum crystals are large (Fig. 9b) and, in some cases,  
639 are still found within the ice (Fig. 9a) and surrounded by milky ice rich in air

640 inclusions (Fig. 9a, e), and iii) boulders are locally overgrown by gypsum (Fig.  
641 9c).

642 Coarse-grained cryogenic cave minerals form in a semi-closed system, when  
643 water freezes very slowly (Žák et al., 2004). Once supersaturation is reached,  
644 CCM start to crystallize. The formation of gypsum crystals requires the presence  
645 of elevated concentrations of dissolved sulfate which may relate to i) sedimentary  
646 gypsum deposits intercalated within carbonates (e.g., Sancho et al., 2004), ii) the  
647 presence of hydrothermal water containing H<sub>2</sub>S related to hydrocarbons (e.g.,  
648 Hill, 1987), or iii) the oxidation of sulfides (e.g., pyrite) disseminated in carbonate  
649 rocks (e.g., Bottrell, 1991). In the case of Devaux cave marine evaporite rocks  
650 (e.g., of the Upper Triassic Keuper facies) and hydrocarbons are absent in the  
651 catchment of the cave. The most plausible explanation for the presence of  
652 dissolved sulfate in Devaux's water is the oxidation of pyrite present in the  
653 limestone (du Cailar and Dubois, 1953; Requirand, 2014).

654

655  $\delta^{34}\text{S}$  values of gypsum (-11.9 to -15.8 ‰), pyrite (-12.7 ‰), and dissolved sulfate  
656 (-14.4 ‰ in dripwater and -28.5 to -27.3 ‰ in Brulle spring water) are within the  
657 range of biogenic pyrite and differ notably from values of marine evaporites (10-  
658 35 ‰) (Seal, 2006). Thus, the  $\delta^{34}\text{S}$  values together with the geological setting of  
659 the cave support the hypothesis that disseminated pyrite in the host limestone is  
660 the main source of dissolved sulfate and subsequently of CCG. Only the  
661 dissolved sulfate  $\delta^{34}\text{S}$  values of Brulle spring are considerably more negative (-  
662 28.5‰ and -27.3‰). This may be a consequence of microbially mediated redox  
663 processes in the karst that discriminate against  $^{34}\text{S}$  (Zerkle et al., 2016; Temovski  
664 et al., 2018). Further studies on the microbiology of the cave may shed light on  
665 these mechanisms and how the local sulfur cycle may have changed in the recent  
666 past.

667

668 In gypsum caves, dissolved sulfate dominates over the bicarbonate, and the  
669 typical crystallization sequence during freezing of water with high TDS is gypsum  
670 → carbonate (commonly calcite) → celestine (Žák et al., 2018). In Devaux cave,  
671 however, bicarbonate dominates over sulfate, and our observations show that  
672 gypsum crystals partly nucleated on CCC<sub>coarse</sub>. Accordingly, the crystallization

673 sequence at Devaux cave is calcite → gypsum, taking place in a semi-closed  
674 system at low freezing rates.

675

676 The second aspect that makes the CCG in Devaux cave unique is the size and  
677 euhedral shapes of the crystals (Fig. 9 b), which differ notably from the much  
678 smaller sizes of gypsum crystals (20-200 μm) and gypsum powders (1-30 μm)  
679 found in gypsum caves in Russia and Ukraine (Žák et al., 2018 and references  
680 therein). Another characteristic of CCC and CCG occurrences in Devaux cave is  
681 the presence of milky ice surrounding them (Fig. 9a, e) which seems to be related  
682 to the freezing process during the formation cryogenic minerals in a subaqueous  
683 environment. Similar to that, CCC were found within the ice and surrounded by  
684 bubbles in Sarrios 6 ice cave (Bartolomé et al., 2015). However, the scarce  
685 presence of CCC within the ice today, together with the very few sites where this  
686 topic is investigated, leads to a lack of studies about gas inclusions and CO<sub>2</sub>  
687 degassing during CCC formation.

688

689 Finally, the presence of gypsum aggregates overgrowing blocks (Fig. 9c)  
690 supports the hypothesis of subaqueous gypsum formation. On the other hand,  
691 the absence of gypsum growing on the ceiling or on the walls allows to discard  
692 its formation from seepage water followed by precipitation due to evaporation in  
693 the cave (e.g., Gázquez et al., 2017, 2020). In essence, all observations indicate  
694 that gypsum precipitated in a semi-closed subaqueous environment and has  
695 been preserved from later dissolution by the exceptionally dry environment of this  
696 ice cave. Gypsum precipitating from freezing waters has been also documented  
697 in the Arctic and the Antarctica (Losiak et al., 2016; Wollenburg et al., 2018) and  
698 has been proposed as a mechanism for gypsum formation on Mars (Losiak et al.,  
699 2016).

700

## 701 **6. Conclusions**

702 The investigation of Devaux ice cave, based on cave monitoring, geomorphology,  
703 and geochemical analyses, provides exceptional insights into the origin of  
704 modern and past mountain permafrost and associated processes and deposits.

705 - Devaux cave consists of two parts characterised by different thermal regimes:  
706 1) the near-entrance parts and the main gallery showing large temperature  
707 fluctuations and cave air temperatures seasonally exceeding 0°C. These  
708 passages are influenced by advective air flow and heat released by the cave  
709 river. 2) The inner sector and isolated chambers are characterized by muted  
710 thermal oscillations and temperatures constantly below 0°C. There, the cave air  
711 temperature is mainly controlled by heat conduction through the bedrock.

712

713 - Devaux cave is impacted by backflooding in late winter/early spring when the  
714 main outlets freeze, damming the water inside the cave forming a lake. The  
715 blocking of the outlets requires temperatures below 0°C in the Gavarnie cirque,  
716 while on the southern side of the Monte Perdido massif, temperatures above  
717 0°C allow water infiltration.

718

719 - The absence of dripwater in most parts of the cave together with the presence  
720 of perennial/seasonal hoarfrost, and the location of massive ice bodies on the  
721 ceiling and/or filling cupulas and galleries are indicative of frozen bedrock  
722 surrounding the cave. Permafrost at Devaux cave is attributed to a combination  
723 of rock undercooling by cave air ventilation and the local climate setting giving  
724 rise to the development and/or preservation of permafrost inherited from past  
725 colder periods. Currently, permafrost seems to be present above the cave  
726 reaching a maximum thickness of ~200 m and a lateral extension of ~350 m  
727 towards the southern face of the Monte Perdido massif.

728

729 - We report the first deposits of cryogenic gypsum in a limestone-hosted ice cave.  
730 Most of the cryogenic minerals are still within the ice and surrounded by milky  
731 ice rich in air inclusions. Gypsum precipitation occurred subaqueously as a  
732 result of slow freezing, following CCC formation.  $\delta^{34}\text{S}$  values show that the  
733 sulfate originated from the oxidation of pyrite present in the limestone.

734

735 - Current climate conditions seem to be still favourable for the preservation of ice  
736 within this cave. This situation contrasts to the large ice mass loss in other ice  
737 caves elsewhere. The ice deposits in Devaux cave allow unique insights into  
738 processes leading to the formation of cryogenic carbonates and sulfates, and

739 represents a unique site to better understand the mountain permafrost evolution  
740 in the Monte Perdido massif and the Pyrenees in general.

#### 741 **Competing interests**

742 No competing of interest

#### 743 **Authors contribution**

744 MB conceived the project, planned fieldwork and the sampling strategy. AM  
745 obtained funding for this work. MB and GC installed and maintained the sensors  
746 and performed the fieldwork. GC contributed with cave monitoring data from 2011  
747 to 2015. MB analysed monitoring, geomorphological, and geochemical data. FG  
748 performed  $\delta^{34}\text{S}$  analyses using the facilities provided by AVT. JILM created the  
749 radiation map. MB designed the figures and wrote a first draft of the manuscript.  
750 ML and CS contributed to the discussion of the data. ML and AM reviewed all  
751 versions of the manuscript. All authors reviewed the manuscript and contributed  
752 to the results, discussion, and final interpretation. All authors approved its  
753 submission.

#### 754 **Acknowledgements**

755 We thank the directorates of the Parc National des Pyrénées (France) and the  
756 Ordesa y Monte Perdido National Park (Spain) for their permission to investigate  
757 Devaux cave. We want to especially thank Marc Galy for his cave survey which  
758 improves noticeably previously published surveys and for the historical photo of  
759 1984. Also, we thank Météo France for providing climate data from the Pic du  
760 midi de Bigorre station. We thank Maria Leunda for a critical review and  
761 suggestions to the first draft of the manuscript. We also thank Jerome Labat  
762 (SSPPO), Claude Novoa, Alvaro Palacios, Maria Leunda, José Leunda, David  
763 Serrano, the Góriz hut staff ([www.goriz.es](http://www.goriz.es)), and the Palazzo family  
764 ([www.hotelpalazio.com](http://www.hotelpalazio.com)) for their invaluable help during fieldwork. We thank Paul  
765 Cluzon for the photo of Fig. 1d, and Claude Requirand for his report about Devaux  
766 cave. The authors would like to acknowledge the use of the Servicio General de  
767 Apoyo a la Investigación-SAI, University of Zaragoza, and Alberto Barcos (IPE-  
768 CSIC) for the chemical water analyses. This study contributes to the work carried  
769 out by the DGA research group Procesos Geoambientales y Cambio Global (ref.:  
770 E02-20R) and the MERS research group 2017 SGR 1588.



771 **Financial support**

772 This research has been supported by the following projects which were funded  
773 by the National Parks Autonomous Agency (OAPN) (OCHESTRA-ref  
774 2552/2020), the Spanish Agencia Estatal de Investigación (AEI-Spain)  
775 (PICACHU-ref PID2019-106050RB-I00), (SPYRIT- ref CGL2016-77479-R), the  
776 PaleoICE EXPLORA project (ref. CGL2015-72167-EXP) and the Comité régional  
777 de spéléologie de Nouvelle Aquitaine. Miguel Bartolomé was supported by a  
778 postdoctoral fellowship of the Juan de la Cierva-Formación program provided by  
779 the Spanish Ministry of Science (ref.: FJCI-2017-31725) and OCHESTRA-ref  
780 2552/2020. Fernando Gázquez was financially supported by a Ramón y Cajal  
781 Fellowship (RYC2020-029811-I) of the Spanish Government (Ministerio de  
782 Economía y Competividad).

783

784 **References**

- 785 Badino, G., 2010. UNDERGROUND METEOROLOGY-“What’s the weather underground?” *Acta*  
786 *Carsologica* 39. <https://doi.org/10.3986/ac.v39i3.74>
- 787 Bartolomé, M., Sancho, C., Benito, G., Medialdea, A., Calle, M., Moreno, A., Leunda, M.,  
788 Luetscher, M., Muñoz, A., Bastida, J., Cheng, H., Edwards, R.L., 2021. Effects of  
789 glaciation on karst hydrology and sedimentology during the Last Glacial Cycle: The case  
790 of Granito cave, Central Pyrenees (Spain). *CATENA* 206, 105252.  
791 <https://doi.org/10.1016/j.catena.2021.105252>
- 792 Bartolomé, M., Sancho, C., Osácar, M.C., Moreno, A., Leunda, M., Spötl, C., Luetscher, M.,  
793 López-Martínez, J., Belmonte, A., 2015. Characteristics of cryogenic carbonates in a  
794 Pyrenean ice cave (northern Spain). *Geogaceta* 58 107–110.
- 795 Belmonte-Ribas, Á., Sancho, C., Moreno, A., Lopez-Martinez, J., Bartolome, M., 2014. Present-  
796 day environmental dynamics in ice cave a294, central pyrenees, spain. *Geogr. Fis. E*  
797 *Din. Quat.* 37, 131–140. <https://doi.org/10.4461/GFDQ.2014.37.12>
- 798 Biskaborn, B.K., Smith, S.L., Noetzli, J., Matthes, H., Vieira, G., Streletskiy, D.A., Schoeneich, P.,  
799 Romanovsky, V.E., Lewkowicz, A.G., Abramov, A., Allard, M., Boike, J., Cable, W.L.,  
800 Christiansen, H.H., Delaloye, R., Diekmann, B., Drozdov, D., Etzelmüller, B., Grosse, G.,  
801 Guglielmin, M., Ingeman-Nielsen, T., Isaksen, K., Ishikawa, M., Johansson, M.,  
802 Johansson, H., Joo, A., Kaverin, D., Kholodov, A., Konstantinov, P., Kröger, T., Lambiel,  
803 C., Lanckman, J.-P., Luo, D., Malkova, G., Meiklejohn, I., Moskalenko, N., Oliva, M.,  
804 Phillips, M., Ramos, M., Sannel, A.B.K., Sergeev, D., Seybold, C., Skryabin, P., Vasiliev,  
805 A., Wu, Q., Yoshikawa, K., Zheleznyak, M., Lantuit, H., 2019. Permafrost is warming at a  
806 global scale. *Nat. Commun.* 10, 264. <https://doi.org/10.1038/s41467-018-08240-4>
- 807 Boeckli, L., Brenning, A., Gruber, S., Noetzli, J., 2012. A statistical approach to modelling  
808 permafrost distribution in the European Alps or similar mountain ranges. *The*  
809 *Cryosphere* 6, 125–140. <https://doi.org/10.5194/tc-6-125-2012>

810 Bottrell, S.H., 1991. Sulphur isotope evidence for the origin of cave evaporites in Ogof y Daren  
811 Cilau, south Wales. *Mineral. Mag.* 55, 209–210.  
812 <https://doi.org/10.1180/minmag.1991.055.379.09>

813 Bücher, A., Dessens, J., 1991. Secular Trend of Surface Temperature at an Elevated  
814 Observatory in the Pyrenees. *J. Clim.* 4, 859–868. [https://doi.org/10.1175/1520-0442\(1991\)004<0859:STOSTA>2.0.CO;2](https://doi.org/10.1175/1520-0442(1991)004<0859:STOSTA>2.0.CO;2)

816 Casteret, N., 1953. Dans les glaces souterraines. Les plus élevées de Monde. Libraire  
817 Académique Perrin, Paris, p. 93.

818 Colucci, R., Luetscher, M., Fortet, E., Guglielmin, M., Lenaz, D., Princivalle, F., Vita, F., 2017.  
819 First alpine evidence of in situ coarse cryogenic cave carbonates (CCCcoarse). *Geogr. Fis. E Din. Quat.* 53–59. <https://doi.org/10.4461/GFDQ.2017.40.5>

820 Colucci, R.R., Guglielmin, M., 2019. Climate change and rapid ice melt: Suggestions from abrupt  
821 permafrost degradation and ice melting in an alpine ice cave. *Prog. Phys. Geogr. Earth Environ.* 0309133319846056. <https://doi.org/10.1177/0309133319846056>

822 Dessens, J., Bücher, A., 1995. Changes in minimum and maximum temperatures at the Pic du  
823 Midi in relation with humidity and cloudiness, 1882–1984. *Atmospheric Res.*, 37, 147–  
824 162. [https://doi.org/10.1016/0169-8095\(94\)00075-0](https://doi.org/10.1016/0169-8095(94)00075-0)

825 Devaux, J., 1929. Nouvelle grotte Marboréenne. *La Natura* 102–107.

826 Devaux, J., 1933. La grotte des sœurs de la cascade. *Études glaciologiques, 1920-1930. Tome VII*, pp. 233-238. Plan & coupe. Paris. Imprimerie Nationale. Ministère de l'Agriculture.  
827 Direction des eaux et du génie rural.

831 du Cailar, J., Couderc, J., Dubois, P., 1953. La source du Gave de Pau. *Annales de Spéléologie*  
832 181–203.

833 du Cailar, J., Dubois, P., 1953. Sur quelques modalités de formation et d'évolution des dépôts  
834 cristallins dans les cavités de haute altitude. In: Premier congrès international de  
835 spéléologie. Paris, Tome II, pp 325-333.

836 Dublyansky, Y., Moseley, G.E., Lyakhnitsky, Y., Cheng, H., Edwards, L.R., Scholz, D., Koltai, G.,  
837 Spötl, C., 2018. Late Palaeolithic cave art and permafrost in the Southern Ural. *Sci. Rep.*  
838 8, 12080. <https://doi.org/10.1038/s41598-018-30049-w>

839 Fankhauser, A., McDermott, F., Fleitmann, D., 2016. Episodic speleothem deposition tracks the  
840 terrestrial impact of millennial-scale last glacial climate variability in SW Ireland. *Quat.*  
841 *Sci. Rev.* 152, 104–117. <https://doi.org/10.1016/j.quascirev.2016.09.019>

842 Feuillet, T., 2011. Statistical Analyses of Active Patterned Ground Occurrence in the Taillon  
843 Massif (Pyrénées, France/Spain). *Permafr. Periglac. Process.* 22, 228–238.  
844 <https://doi.org/10.1002/ppp.726>

845 García-Ruiz, J.M., Palacios, D., Andrés, N. de, Valero-Garcés, B.L., López-Moreno, J.I., Sanjuán,  
846 Y., 2014. Holocene and 'Little Ice Age' glacial activity in the Marboré Cirque, Monte  
847 Perdido Massif, Central Spanish Pyrenees. *The Holocene* 24, 1439–1452.  
848 <https://doi.org/10.1177/0959683614544053>

849 García-Ruiz, J.M., Palacios, D., Andrés, N., López-Moreno, J.I., 2020. Neoglaciation in the  
850 Spanish Pyrenees: a multiproxy challenge. *Mediterr. Geosci. Rev.* 2, 21–36.  
851 <https://doi.org/10.1007/s42990-020-00022-9>

852 Gázquez, F., Bauska, T.K., Comas-Bru, L., Ghaleb, B., Calaforra, J.-M., Hodell, D.A., 2020. The  
853 potential of gypsum speleothems for paleoclimatology: application to the Iberian  
854 Roman Humid Period. *Sci. Rep.* 10, 14705. <https://doi.org/10.1038/s41598-020-71679-3>

855

856 Gázquez, F., Calaforra, J.M., Evans, N.P., Hodell, D.A., 2017. Using stable isotopes ( $\delta^{17}\text{O}$ ,  $\delta^{18}\text{O}$   
857 and  $\delta\text{D}$ ) of gypsum hydration water to ascertain the role of water condensation in the  
858 formation of subaerial gypsum speleothems. *Chem. Geol.* 452, 34–46.  
859 <https://doi.org/10.1016/j.chemgeo.2017.01.021>

- 860 Gellatly, A.F., Grove, J.M., Switsur, V.R., 1992. Mid-Holocene glacial activity in the Pyrenees.  
861 The Holocene 2, 266–270. <https://doi.org/10.1177/095968369200200309>
- 862 Gieseemann, A., Jaeger, H.-J., Norman, A.L., Krouse, H.R., Brand, W.A., 1994. Online Sulfur-  
863 Isotope Determination Using an Elemental Analyzer Coupled to a Mass Spectrometer.  
864 Anal. Chem. 66, 2816–2819. <https://doi.org/10.1021/ac00090a005>
- 865 Gomez Lende, M., Berenguer, F., Serrano, E., 2014. Morphology, ice types and thermal regime  
866 in a high mountain ice cave. First studies applying terrestrial laser scanner in the Peña  
867 Castil ice cave (Picos de Europa, Northern Spain). Geogr. Fis. E Din. Quat. 37, 141–150.  
868 <https://doi.org/10.4461/GFDQ.2014.37.13>
- 869 Gómez Lende, M., Serrano, E., Bordehore, L.J., Sandoval, S., 2016. The role of GPR techniques  
870 in determining ice cave properties: Peña Castil ice cave, Picos de Europa. Earth Surf.  
871 Process. Landf. 41, 2177–2190. <https://doi.org/10.1002/esp.3976>
- 872 Gómez-Ortiz, A., Oliva, M., Salvador-Franch, F., Palacios, D., Tanarro, L.M., de Sanjosé-Blasco,  
873 J.J., Salvà-Catarineu, M., 2019. Monitoring permafrost and periglacial processes in  
874 Sierra Nevada (Spain) from 2001 to 2016. Permafr. Periglac. Process. 30, 278–291.  
875 <https://doi.org/10.1002/ppp.2002>
- 876 González Trueba, J.J., Moreno, R.M., Martínez de Pisón, E., Serrano, E., 2008. ‘Little Ice Age’  
877 glaciation and current glaciers in the Iberian Peninsula. The Holocene 18, 551–568.  
878 <https://doi.org/10.1177/0959683608089209>
- 879 Gruber, S., Haeberli, W., 2009. Mountain Permafrost, in: Margesin, R. (Ed.), Permafrost Soils,  
880 Soil Biology. Springer, Berlin, Heidelberg, pp. 33–44. [https://doi.org/10.1007/978-3-540-69371-0\\_3](https://doi.org/10.1007/978-3-540-69371-0_3)
- 882 Gubler, S., Fiddes, J., Keller, M., Gruber, S., 2011. Scale-dependent measurement and analysis  
883 of ground surface temperature variability in alpine terrain. The Cryosphere 5, 431–443.  
884 <https://doi.org/10.5194/tc-5-431-2011>
- 885 Haeberli, W., Rellstab, W., Harrison, W.D., 1984. Geothermal Effects of 18 ka BP Ice Conditions  
886 in the Swiss Plateau. Ann. Glaciol. 5, 56–60. <https://doi.org/10.3189/1984AoG5-1-56-60>
- 888 Harris, C., Vonder Mühl, D., Isaksen, K., Haeberli, W., Sollid, J.L., King, L., Holmlund, P., Dramis,  
889 F., Guglielmin, M., Palacios, D., 2003. Warming permafrost in European mountains.  
890 Glob. Planet. Change 39, 215–225. <https://doi.org/10.1016/j.gloplacha.2003.04.001>
- 891 Heeb, B., 2014. The Next Generation of the DistoX Cave Surveying Instrument. CREG J., 88, 5-8.
- 892 Hercman, H., Gašiorowski, M., Gradziński, M., Kicińska, D., 2010. The First Dating of Cave Ice  
893 from the Tatra Mountains, Poland and its Implication to Palaeoclimate  
894 Reconstructions. Geochronometria 36, 31–38. <https://doi.org/10.2478/v10003-010-0016-2>
- 896 Hill, C.A., 1987. Geology of Carlsbad Cavern and other caves in the Guadalupe Mountains, New  
897 Mexico and Texas. Bull 117 N. M. Bur. Mines Miner. Resour.
- 898 Hock, R., Rasul, G., Adler, C., Cáceres, B., Gruber, S., Hirabayashi, Y., Jackson, J., Käab, A., Kang,  
899 S., Kutuzov, S., Milner, A., Molau, U., Morin, S., Orlove, B., Steltzer, H., 2019. High  
900 Mountain Areas. In: IPCC Special Report on the Ocean and Cryosphere in a Changing  
901 Climate.
- 902 Kern, Z., Bočić, N., Sipos, G., 2018. Radiocarbon-Dated Vegetal Remains from the Cave Ice  
903 Deposits of Velebit Mountain, Croatia. Radiocarbon 60, 1391–1402.  
904 <https://doi.org/10.1017/RDC.2018.108>
- 905 Kern, Z., Perşoiu, A., 2013. Cave ice – the imminent loss of untapped mid-latitude cryospheric  
906 palaeoenvironmental archives. Quat. Sci. Rev. 67, 1–7.  
907 <https://doi.org/10.1016/j.quascirev.2013.01.008>
- 908 Koltai, G., Spötl, C., Cheng, H., 2020. Cryogenic cave carbonates in the Dolomites (Northern  
909 Italy): insights into Younger Dryas cooling and seasonal precipitation. Clim. Past  
910 Discuss. 1–25. <https://doi.org/10.5194/cp-2020-107>

- 911 Korshunov, V.V., Shavrina, E.V., 1998. Gypsum speleothems of freezing origin. *J. Cave Karst*  
912 *Stud.* 60, 146–150.
- 913 Lechleitner, F.A., Mason, A.J., Breitenbach, S.F.M., Vaks, A., Haghypour, N., Henderson, G.M.,  
914 2020. Permafrost-related hiatuses in stalagmites: Evaluating the potential for  
915 reconstruction of carbon cycle dynamics. *Quat. Geochronol.* 56, 101037.  
916 <https://doi.org/10.1016/j.quageo.2019.101037>
- 917 Leunda, M., González-Sampériz, P., Gil-Romera, G., Bartolomé, M., Belmonte-Ribas, Á., Gómez-  
918 García, D., Kaltenrieder, P., Rubiales, J.M., Schwörer, C., Tinner, W., Morales-Molino,  
919 C., Sancho, C., 2019. Ice cave reveals environmental forcing of long-term Pyrenean tree  
920 line dynamics. *J. Ecol.* 107, 814–828. <https://doi.org/10.1111/1365-2745.13077>
- 921 Lewkowicz, A.G., Ednie, M., 2004. Probability mapping of mountain permafrost using the BTS  
922 method, Wolf Creek, Yukon Territory, Canada. *Permafr. Periglac. Process.* 15, 67–80.  
923 <https://doi.org/10.1002/ppp.480>
- 924 Li, T.-Y., Baker, J.L., Wang, T., Zhang, J., Wu, Y., Li, H.-C., Blyakharchuk, T., Yu, T.-L., Shen, C.-C.,  
925 Cheng, H., Kong, X.-G., Xie, W.-L., Edwards, R.L., 2021. Early Holocene permafrost  
926 retreat in West Siberia amplified by reorganization of westerly wind systems.  
927 *Commun. Earth Environ.* 2, 1–11. <https://doi.org/10.1038/s43247-021-00238-z>
- 928 López-Moreno, J.I., Alonso-González, E., Monserrat, O., Del Río, L.M., Otero, J., Lapazaran, J.,  
929 Luzi, G., Dematteis, N., Serreta, A., Rico, I., Serrano-Cañadas, E., Bartolomé, M.,  
930 Moreno, A., Buisan, S., Revuelto, J., 2019. Ground-based remote-sensing techniques  
931 for diagnosis of the current state and recent evolution of the Monte Perdido Glacier,  
932 Spanish Pyrenees. *J. Glaciol.* 65, 85–100. <https://doi.org/10.1017/jog.2018.96>
- 933 López-Moreno, J.I., Revuelto, J., Rico, I., Chueca-Cía, J., Julián, A., Serreta, A., Serrano, E.,  
934 Vicente-Serrano, S.M., Azorin-Molina, C., Alonso-González, E., García-Ruiz, J.M., 2016.  
935 Thinning of the Monte Perdido Glacier in the Spanish Pyrenees since 1981. *The*  
936 *Cryosphere* 10, 681–694. <https://doi.org/10.5194/tc-10-681-2016>
- 937 Losiak, A., Derkowski, A., Skała, A., Trzciński, J., 2016. Evaporites on ice: how to form gypsum  
938 on Antarctica and on Martian North polar residual cap? In: 47th Lunar and Planetary  
939 Science Conference. 1972.pdf.
- 940 Luetscher, M., Bolius, D., Schwikowski, M., Schotterer, U., Smart, P.L., 2007. Comparison of  
941 techniques for dating of subsurface ice from Monlesi ice cave, Switzerland. *J. Glaciol.*  
942 53, 374–384.
- 943 Luetscher, M., Borreguero, M., Moseley, G.E., Spötl, C., Edwards, R.L., 2013. Alpine permafrost  
944 thawing during the Medieval Warm Period identified from cryogenic cave carbonates.  
945 *The Cryosphere* 7, 1073–1081. <https://doi.org/10.5194/tc-7-1073-2013>
- 946 Luetscher, M., Jeannin, P.-Y., 2018. Chapter 12 - Ice Caves in Switzerland, in: Perşoiu, A.,  
947 Lauritzen, S.-E. (Eds.), *Ice Caves*. Elsevier, pp. 221–235. <https://doi.org/10.1016/B978-0-12-811739-2.00010-3>
- 949 Luetscher, M., Lismonde, B., Jeannin, P.-Y., 2008. Heat exchanges in the heterothermic zone of  
950 a karst system: Monlesi cave, Swiss Jura Mountains. *J. Geophys. Res. Earth Surf.* 113.  
951 <https://doi.org/10.1029/2007JF000892>
- 952 Lundberg, J., McFarlane, D.A., 2007. Pleistocene depositional history in a periglacial terrane: A  
953 500 k.y. record from Kents Cavern, Devon, United Kingdom. *Geosphere* 3, 199–219.  
954 <https://doi.org/10.1130/GES00085.1>
- 955 Marshall, P., Brown, M.C., 1974. Ice in Coulthard Cave, Alberta. *Can. J. Earth Sci.*  
956 <https://doi.org/10.1139/e74-045>
- 957 Mavlyudov, B.R., 2008. Caves Glaciation in the Past. Федеральное государственное  
958 бюджетное учреждение науки Институт географии Российской академии наук, pp.  
959 499–505.
- 960 Moseley, G.E., Edwards, R.L., Lord, N.S., Spötl, C., Cheng, H., 2021. Speleothem record of mild  
961 and wet mid-Pleistocene climate in northeast Greenland. *Sci. Adv.* 7, eabe1260.  
962 <https://doi.org/10.1126/sciadv.abe1260>

963 Munroe, J., Kimble, K., Spötl, C., Marks, G.S., McGee, D., Herron, D., 2021. Cryogenic cave  
964 carbonate and implications for thawing permafrost at Winter Wonderland Cave, Utah,  
965 USA. *Sci. Rep.* 11, 6430. <https://doi.org/10.1038/s41598-021-85658-9>  
966 Munroe, J.S., 2021. First investigation of perennial ice in Winter Wonderland Cave, Uinta  
967 Mountains, Utah, USA. *The Cryosphere* 15, 863–881. <https://doi.org/10.5194/tc-15-863-2021>  
968 Navarro-Serrano, F., López-Moreno, J.I., Azorin-Molina, C., Alonso-González, E., Tomás-  
969 Burguera, M., Sanmiguel-Valladolid, A., Revuelto, J., Vicente-Serrano, S.M., 2018.  
970 Estimation of near-surface air temperature lapse rates over continental Spain and its  
971 mountain areas. *Int. J. Climatol.* 38, 3233–3249. <https://doi.org/10.1002/joc.5497>  
972 Noetzli, J., Gruber, S., 2009. Transient thermal effects in Alpine permafrost. *The Cryosphere* 3,  
973 85–99. <https://doi.org/10.5194/tc-3-85-2009>  
974 Orvošová, M., Deininger, M., Milovský, R., 2014. Permafrost occurrence during the Last  
975 Permafrost Maximum in the Western Carpathian Mountains of Slovakia as inferred  
976 from cryogenic cave carbonate. *Boreas* 43, 750–758.  
977 <https://doi.org/10.1111/bor.12042>  
978 Perşoiu, A., Buzjak, N., Onaca, A., Pennos, C., Sotiriadis, Y., Ionita, M., Zachariadis, S., Styllas,  
979 M., Kosutnik, J., Hegyi, A., Butorac, V., 2021. Record summer rains in 2019 led to  
980 massive loss of surface and cave ice in SE Europe. *The Cryosphere* 15, 2383–2399.  
981 <https://doi.org/10.5194/tc-15-2383-2021>  
982 Perşoiu, A., Lauritzen, S.-E. (Eds.), 2018. *Ice caves*. Elsevier, Amsterdam, Netherlands.  
983 Perşoiu, A., Onac, B.P., Wynn, J.G., Blaauw, M., Ionita, M., Hansson, M., 2017. Holocene winter  
984 climate variability in Central and Eastern Europe. *Sci. Rep.* 7, 1196.  
985 <https://doi.org/10.1038/s41598-017-01397-w>  
986 Pons, X., Ninyerola, M., 2008. Mapping a topographic global solar radiation model  
987 implemented in a GIS and refined with ground data. *Int. J. Climatol.* 28, 1821–1834.  
988 <https://doi.org/10.1002/joc.1676>  
989 Racine, T.M.F., Spötl, C., Reimer, P.J., Čarga, J., 2022. RADIOCARBON CONSTRAINTS ON  
990 PERIODS OF POSITIVE CAVE ICE MASS BALANCE DURING THE LAST MILLENNIUM,  
991 JULIAN ALPS (NW SLOVENIA). *Radiocarbon* 1–24.  
992 <https://doi.org/10.1017/RDC.2022.26>  
993 Reille, M., Andrieu, V., 1995. The late Pleistocene and Holocene in the Lourdes Basin, Western  
994 Pyrénées, France: new pollen analytical and chronological data. *Veg. Hist.*  
995 *Archaeobotany* 4, 1–21. <https://doi.org/10.1007/BF00198611>  
996 Requirand, C., 2014. Hypothèse sur la formation des cristaux de gypse Grotte Glacée Devaux  
997 (Gavarnie - Hautes Pyrénées). *Bulletin de la Société Ramon.* 11 pp.  
998 Richter, D.K., Meissner, P., Immenhauser, A., Schulte, U., Dorsten, I., 2010a. Cryogenic and  
1000 non-cryogenic pool calcites indicating permafrost and non-permafrost periods: a case  
1001 study from the Herbstlabyrinth-Advent Cave system (Germany). *The Cryosphere* 4,  
1002 501–509. <https://doi.org/10.5194/tc-4-501-2010>  
1003 Richter, D.K., Meissner, P., Immenhauser, A., Schulte, U., Dorsten, I., 2010b. Cryogenic and  
1004 non-cryogenic pool calcites indicating permafrost and non-permafrost periods: a case  
1005 study from the Herbstlabyrinth-Advent Cave system (Germany). *The Cryosphere* 4,  
1006 501–509. <https://doi.org/10.5194/tc-4-501-2010>  
1007 Rico, I., Magnin, F., López Moreno, J.I., Serrano, E., Alonso-González, E., Revuelto, J., Hughes-  
1008 Allen, L., Gómez-Lende, M., 2021. First evidence of rock wall permafrost in the  
1009 Pyrenees (Vignemale peak, 3,298 m a.s.l., 42°46′16″N/0°08′33″W). *Permafr. Periglac.*  
1010 *Process.* 32, 673–680. <https://doi.org/10.1002/ppp.2130>  
1011 Rodríguez-Salgado, P., Oms, O., Ibáñez-Insa, J., Anadón, P., Gómez de Soler, B., Campeny, G.,  
1012 Agustí, J., 2021. Mineralogical proxies of a Pliocene maar lake recording changes in  
1013 precipitation at the Camp dels Ninots (Pliocene, NE Iberia). *Sediment. Geol.* 418,  
1014 105910. <https://doi.org/10.1016/j.sedgeo.2021.105910>

- 1015 Rösch, G., Rösch, J., 1935. Visites à la grotte Devaux. La Montagne. Revue du Club Alpin  
1016 Français, N° 269, pp.171-178.
- 1017 Rösch, J., 1949. Une exploration de la Grotte Devaux à Gavarnie. Bulletin de la section du Sud-  
1018 Ouest de la Club Alpin Français, N°69. pp. 103-107.
- 1019 Sancho, C., Arenas, C., Pardo, G., Peña-Monné, J.L., Rhodes, E.J., Bartolomé, M., García-Ruiz,  
1020 J.M., Martí-Bono, C., 2018a. Glaciolacustrine deposits formed in an ice-dammed  
1021 tributary valley in the south-central Pyrenees: New evidence for late Pleistocene  
1022 climate. *Sediment. Geol.* 366, 47–66. <https://doi.org/10.1016/j.sedgeo.2018.01.008>
- 1023 Sancho, C., Belmonte, Á., Bartolomé, M., Moreno, A., Leunda, M., López-Martínez, J., 2018b.  
1024 Middle-to-late Holocene palaeoenvironmental reconstruction from the A294 ice-cave  
1025 record (Central Pyrenees, northern Spain). *Earth Planet. Sci. Lett.* 484, 135–144.  
1026 <https://doi.org/10.1016/j.epsl.2017.12.027>
- 1027 Sancho, C., Peña, J.L., Mikkan, R., Osácar, C., Quinif, Y., 2004. Morphological and speleothemic  
1028 development in Brujas Cave (Southern Andean Range, Argentine):  
1029 palaeoenvironmental significance. *Geomorphology* 57, 367–384.  
1030 [https://doi.org/10.1016/S0169-555X\(03\)00166-1](https://doi.org/10.1016/S0169-555X(03)00166-1)
- 1031 Scandroglio, R., Draebing, D., Offer, M., Krautblatter, M., 2021. 4D quantification of alpine  
1032 permafrost degradation in steep rock walls using a laboratory-calibrated electrical  
1033 resistivity tomography approach. *Surf. Geophys.* 19, 241–260.  
1034 <https://doi.org/10.1002/nsg.12149>
- 1035 Seal, R.R., II, 2006. Sulfur Isotope Geochemistry of Sulfide Minerals. *Rev. Mineral. Geochem.*  
1036 61, 633–677. <https://doi.org/10.2138/rmg.2006.61.12>
- 1037 Serrano, E., Gómez-Lende, M., Belmonte, Á., Sancho, C., Sánchez-Benítez, J., Bartolomé, M.,  
1038 Leunda, M., Moreno, A., Hivert, B., 2018. Chapter 28 - Ice Caves in Spain, in: Perşoiu,  
1039 A., Lauritzen, S.-E. (Eds.), *Ice Caves*. Elsevier, pp. 625–655.  
1040 <https://doi.org/10.1016/B978-0-12-811739-2.00028-0>
- 1041 Serrano, E., López-Moreno, J.I., Gómez-Lende, M., Pisabarro, A., Martín-Moreno, R., Rico, I.,  
1042 Alonso-González, E., 2020. Frozen ground and periglacial processes relationship in  
1043 temperate high mountains: a case study at Monte Perdido-Tucarroya area (The  
1044 Pyrenees, Spain). *J. Mt. Sci.* 17, 1013–1031. [https://doi.org/10.1007/s11629-019-5614-](https://doi.org/10.1007/s11629-019-5614-5)  
1045 5
- 1046 Serrano, E., Sanjosé-Blasco, J.J. de, Gómez-Lende, M., López-Moreno, J.I., Pisabarro, A.,  
1047 Martínez-Fernández, A., 2019. Periglacial environments and frozen ground in the  
1048 central Pyrenean high mountain area: Ground thermal regime and distribution of  
1049 landforms and processes. *Permafr. Periglac. Process.* 30, 292–309.  
1050 <https://doi.org/10.1002/ppp.2032>
- 1051 Spötl, C., Cheng, H., 2014. Holocene climate change, permafrost and cryogenic carbonate  
1052 formation: insights from a recently deglaciated, high-elevation cave in the Austrian  
1053 Alps. *Clim. Past* 10, 1349–1362. <https://doi.org/10.5194/cp-10-1349-2014>
- 1054 Spötl, C., Koltai, G., Jarosch, A.H., Cheng, H., 2021. Increased autumn and winter precipitation  
1055 during the Last Glacial Maximum in the European Alps. *Nat. Commun.* 12, 1839.  
1056 <https://doi.org/10.1038/s41467-021-22090-7>
- 1057 Spötl, C., Reimer, P.J., Luetscher, M., 2014. Long-term mass balance of perennial firn and ice in  
1058 an Alpine cave (Austria): Constraints from radiocarbon-dated wood fragments. *The*  
1059 *Holocene* 0959683613515729. <https://doi.org/10.1177/0959683613515729>
- 1060 Stoffel, M., Luetscher, M., Bollschweiler, M., Schlatter, F., 2009. Evidence of NAO control on  
1061 subsurface ice accumulation in a 1200 yr old cave-ice sequence, St. Livres ice cave,  
1062 Switzerland. *Quat. Res.* 72, 16–26. <https://doi.org/10.1016/j.yqres.2009.03.002>
- 1063 Supper, R., Ottowitz, D., Jochum, B., Römer, A., Pfeiler, S., Kauer, S., Keuschnig, M., Ita, A.,  
1064 2014. Geoelectrical monitoring of frozen ground and permafrost in alpine areas: field  
1065 studies and considerations towards an improved measuring technology. *Surf. Geophys.*  
1066 12, 93–115. <https://doi.org/10.3997/1873-0604.2013057>

1067 Temovski, M., Futó, I., Túri, M., Palcsu, L., 2018. Sulfur and oxygen isotopes in the gypsum  
1068 deposits of the Provalata sulfuric acid cave (Macedonia). *Geomorphology* 315, 80–90.  
1069 <https://doi.org/10.1016/j.geomorph.2018.05.010>

1070 Vaks, A., Gutareva, O.S., Breitenbach, S.F.M., Avirmed, E., Mason, A.J., Thomas, A.L., Osinzev,  
1071 A.V., Kononov, A.M., Henderson, G.M., 2013. Speleothems Reveal 500,000-Year  
1072 History of Siberian Permafrost. *Science* 340, 183–186.  
1073 <https://doi.org/10.1126/science.1228729>

1074 Vaks, A., Mason, A.J., Breitenbach, S.F.M., Kononov, A.M., Osinzev, A.V., Rosensaft, M.,  
1075 Borshevsky, A., Gutareva, O.S., Henderson, G.M., 2020. Palaeoclimate evidence of  
1076 vulnerable permafrost during times of low sea ice. *Nature* 577, 221–225.  
1077 <https://doi.org/10.1038/s41586-019-1880-1>

1078 Wind, M., Obleitner, F., Racine, T., Spötl, C., 2022. Multi-annual temperature evolution and  
1079 implications for cave ice development in a sag-type ice cave in the Austrian Alps.  
1080 *Cryosphere Discuss.* 1–26. <https://doi.org/10.5194/tc-2022-67>

1081 Wollenburg, J.E., Katlein, C., Nehrke, G., Nöthig, E.-M., Matthiessen, J., Wolf- Gladrow, D.A.,  
1082 Nikolopoulos, A., Gázquez-Sánchez, F., Rossmann, L., Assmy, P., Babin, M., Bruyant, F.,  
1083 Beaulieu, M., Dybwad, C., Peeken, I., 2018. Ballasting by cryogenic gypsum enhances  
1084 carbon export in a *Phaeocystis* under-ice bloom. *Sci. Rep.* 8, 7703.  
1085 <https://doi.org/10.1038/s41598-018-26016-0>

1086 Yonge, C.J., Ford, D., Horne, G., Lauriol, B., Schroeder, J., 2018. Chapter 15 - Ice Caves in  
1087 Canada, in: Perşoiu, A., Lauritzen, S.-E. (Eds.), *Ice Caves*. Elsevier, pp. 285–334.  
1088 <https://doi.org/10.1016/B978-0-12-811739-2.00015-2>

1089 Žák, K., Onac, B.P., Kadebskaya, O.I., Filippi, M., Dublyansky, Y., Luetscher, M., 2018. Chapter 6  
1090 - Cryogenic Mineral Formation in Caves, in: Perşoiu, A., Lauritzen, S.-E. (Eds.), *Ice  
1091 Caves*. Elsevier, pp. 123–162. <https://doi.org/10.1016/B978-0-12-811739-2.00035-8>

1092 Žák, K., Richter, D.K., Filippi, M., Živor, R., Deininger, M., Mangini, A., Scholz, D., 2012. Coarsely  
1093 crystalline cryogenic cave carbonate – a new archive to estimate the Last  
1094 Glacial minimum permafrost depth in Central Europe. *Clim. Past* 8, 1821–1837.  
1095 <https://doi.org/10.5194/cp-8-1821-2012>

1096 Žák, K., Urban, J., Cílek, V., Hercman, H., 2004. Cryogenic cave calcite from several Central  
1097 European caves: age, carbon and oxygen isotopes and a genetic model. *Chem. Geol.*  
1098 206, 119–136. <https://doi.org/10.1016/j.chemgeo.2004.01.012>

1099 Zerkle, A.L., Jones, D.S., Farquhar, J., Macalady, J.L., 2016. Sulfur isotope values in the sulfidic  
1100 Frasassi cave system, central Italy: A case study of a chemolithotrophic S-based  
1101 ecosystem. *Geochim. Cosmochim. Acta* 173, 373–386.  
1102 <https://doi.org/10.1016/j.gca.2015.10.028>



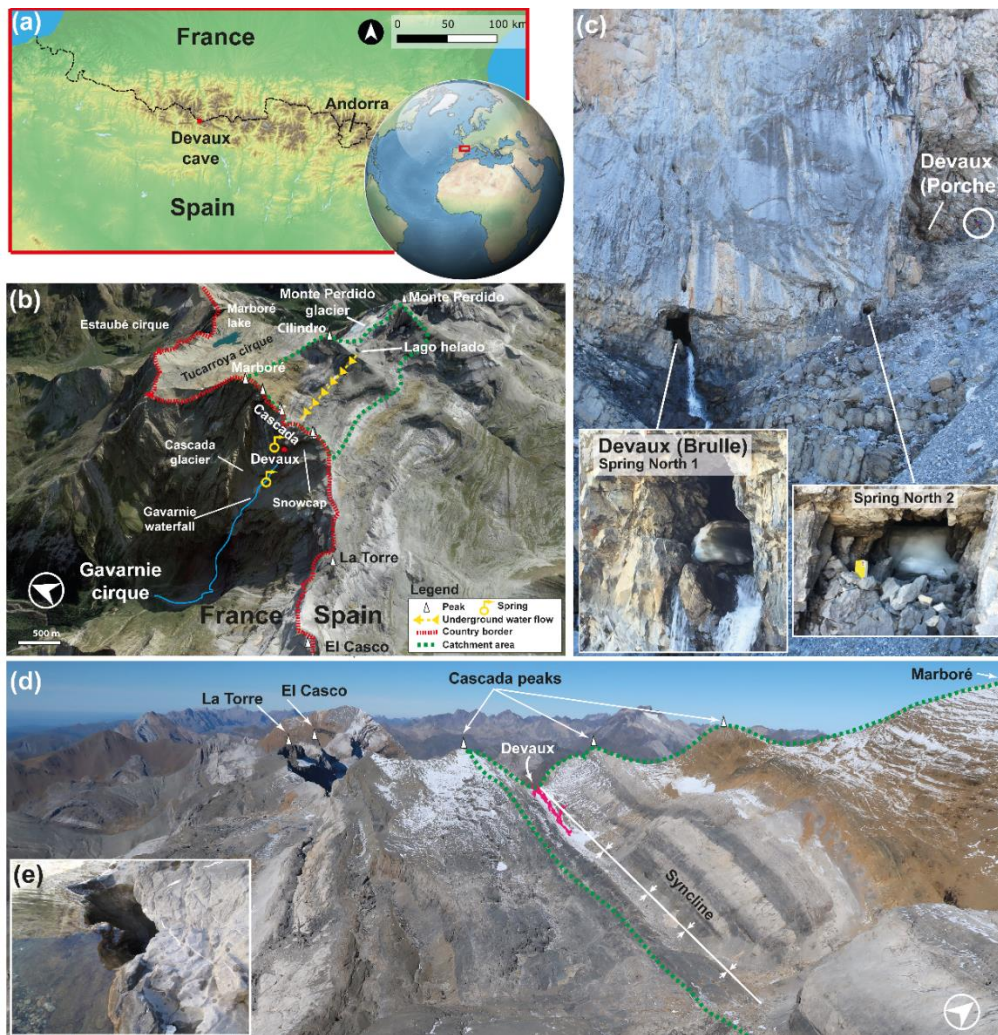


Figure 1. (a) Location of Devaux cave in the Central Pyrenees (ASTER GDEM, NASA v3, 2019). (b) Satellite image and location of Devaux cave, main peaks, lakes, glaciers and cirques in the study area (3D ©Google Earth). The yellow arrows indicate the underground flow path from Lago helado to the Gavarnie waterfall according to the dye-tracing experiment of du Cailar et al., (1953). (c) View towards the entrances of Devaux cave. The lower entrance (~2821 m a.s.l.) corresponds to the Brulle spring (Spring North 1), while the upper one corresponds to the main entrance (Porche (South), ~2836 m a.s.l.). Spring North 2 is located between both entrances. Note person for scale (within the white circle). Remnants of ice partially blocking Brulle and Spring North 2 (July 2021). (d) Landscape view of the catchment area and approximate location of Devaux cave (in dark pink; photo: Paul Cluzon). (e) Ponor located on the southern shore of Lago Helado.



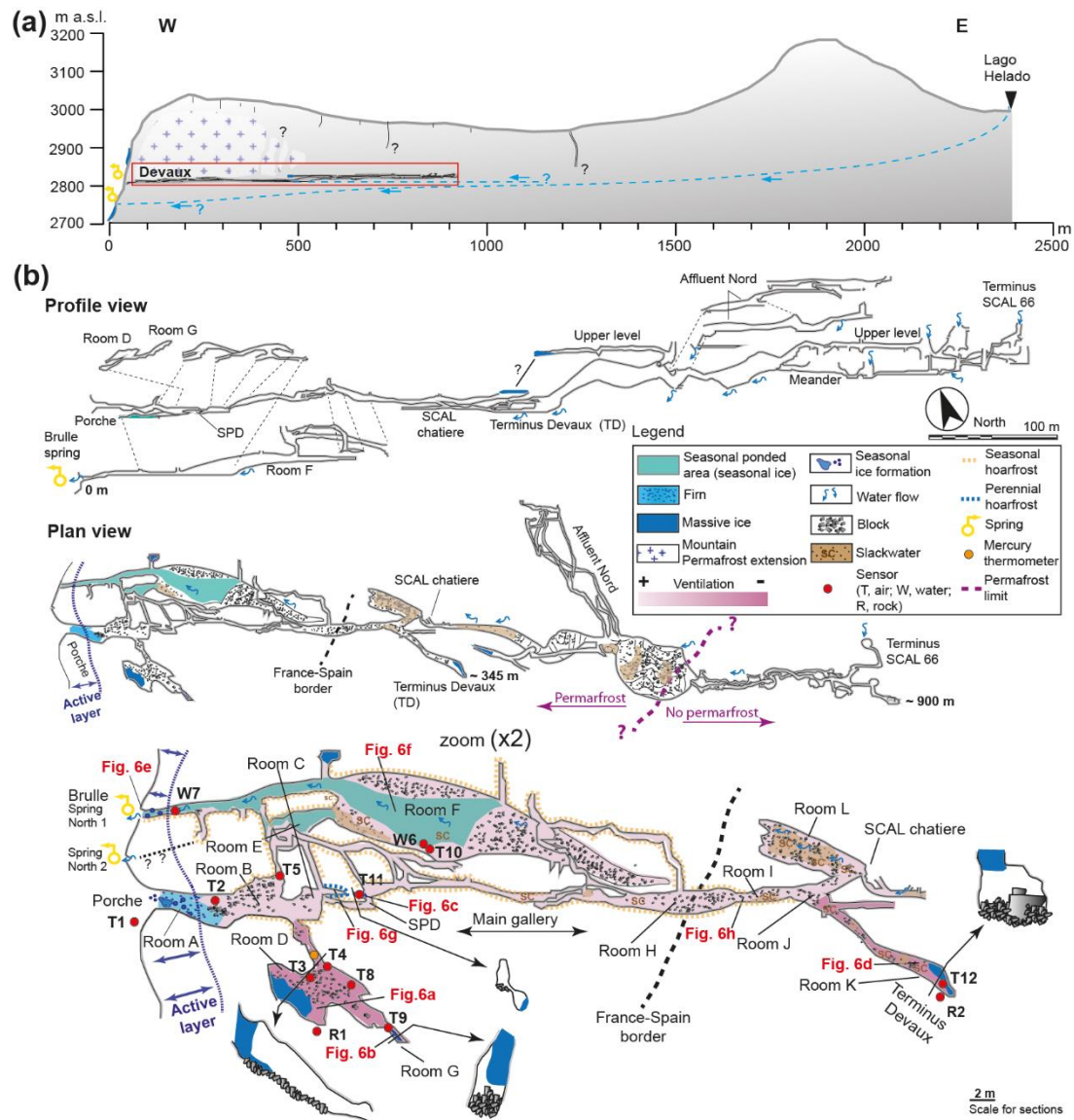


Figure 2. (a) Schematic W-E cross section from Lago helado to Devaux cave, the assumed extent of mountain permafrost, and the interpreted underground flow path according to du Cailar et al., (1953). (b) Longitudinal section and plan view of Devaux cave showing the locations of sensors and cave deposits. Labels R, W and T refer to rock, water and air temperature sensors, respectively. The enlarged area corresponds to the first ~345 m of the studied sector. Red labels correspond to the approximate location of the photographs in Fig. 6. Cave survey by Marc Galy, Groupe Spéléologique des Pyrénées (GSPY 86).

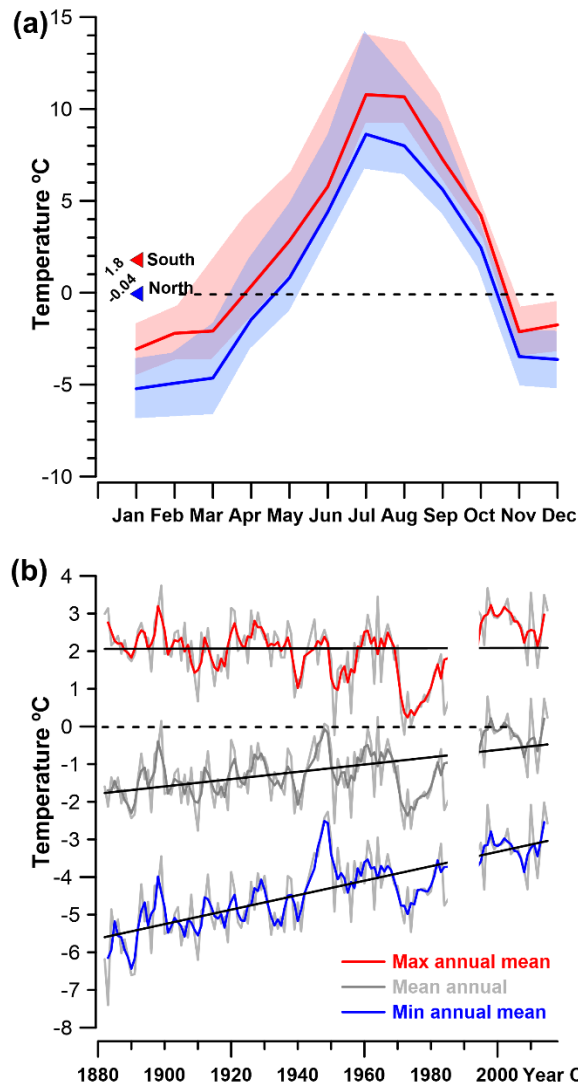


Figure 3. (a) Monthly temperature variation on the northern and southern side of the Monte Perdido massif. Red and blue triangles correspond to the 4-year means. The dashed black line indicates 0°C. Light red and blue shaded envelopes represent the maximum and minimum mean monthly temperatures, respectively. (b) Maximum, mean and minimum annual temperatures recorded at the Pic du Midi de Bigorre station since 1882. Black line indicates the general trend and dashed black line corresponds to 0°C.

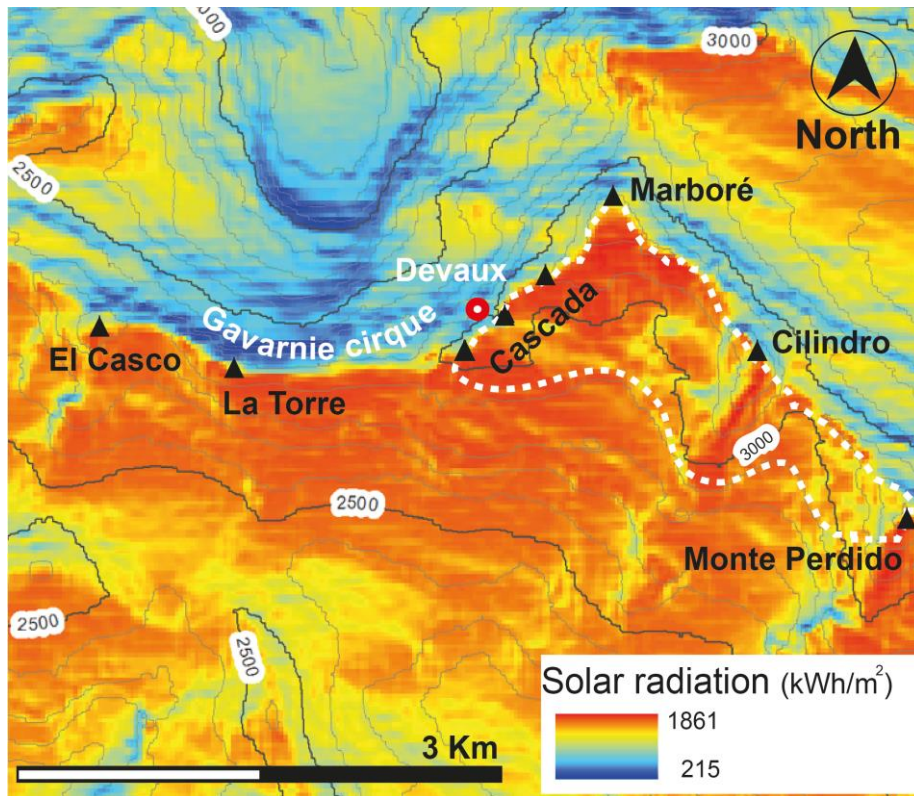


Figure 4. Solar radiation map of the study area. The solar radiation anomaly observed in the Gavarnie cirque is explained by its northerly orientation and the cirque morphology. Black triangles indicate the main peaks above 3000 m. The red-white circle marks Devaux cave, while the dashed white line delineates the approximate catchment.

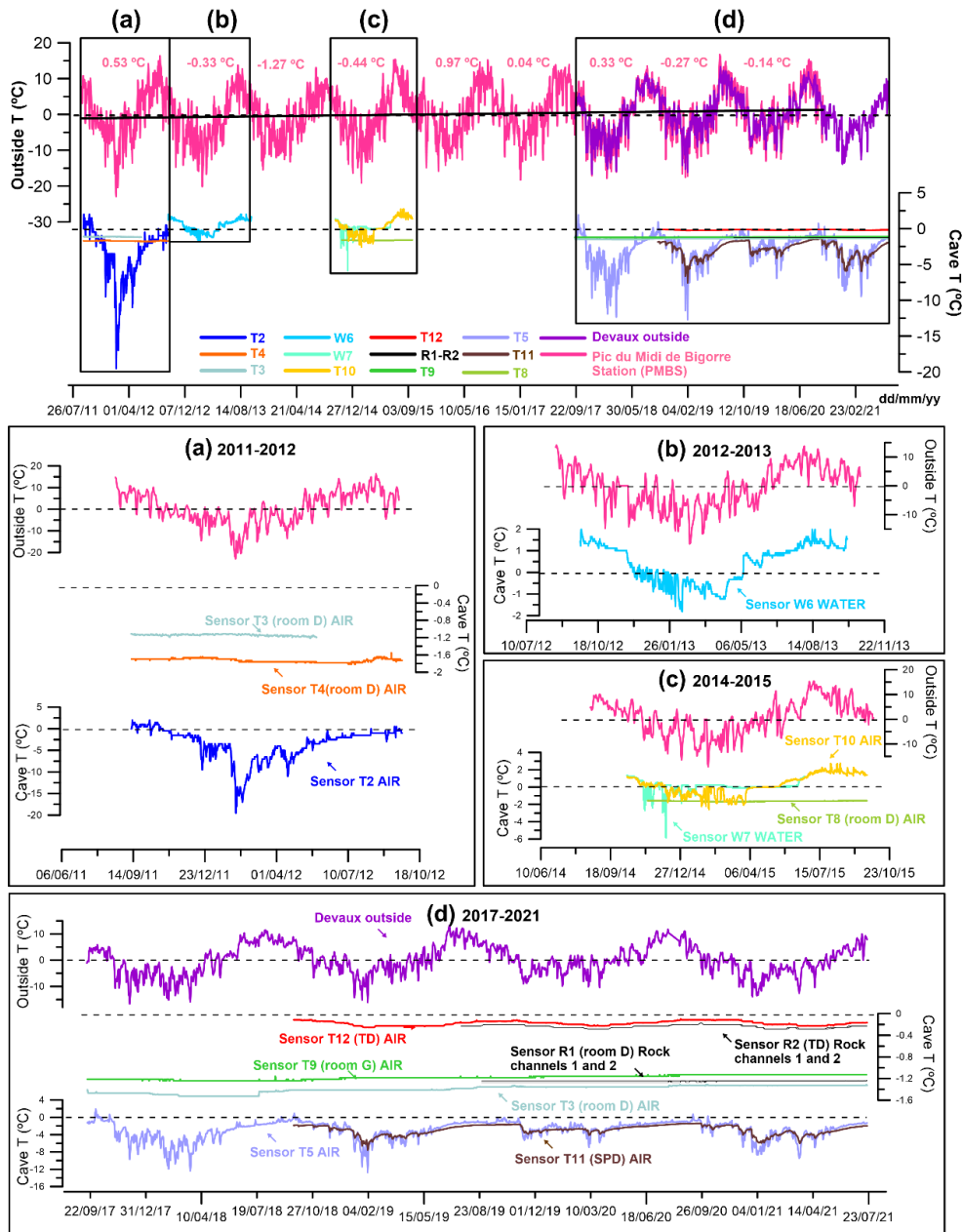


Figure 5. Mean daily air temperature variations at the Pic du Midi de Bigorre station (2860 m a.s.l., red), daily outside air temperature at Devaux cave (2836 m a.s.l., purple) and temperature variations in air, water and rock in the cave for the different time windows since 2011. Dark pink numbers are mean annual air temperatures (MAAT) at the Pic du Midi de Bigorre station (PMBS). Dashed lines indicate 0 °C. Black squares labelled a, b, c, and d correspond to the areas enlarged below. The black continuous line is the external temperature trend during the monitoring period.



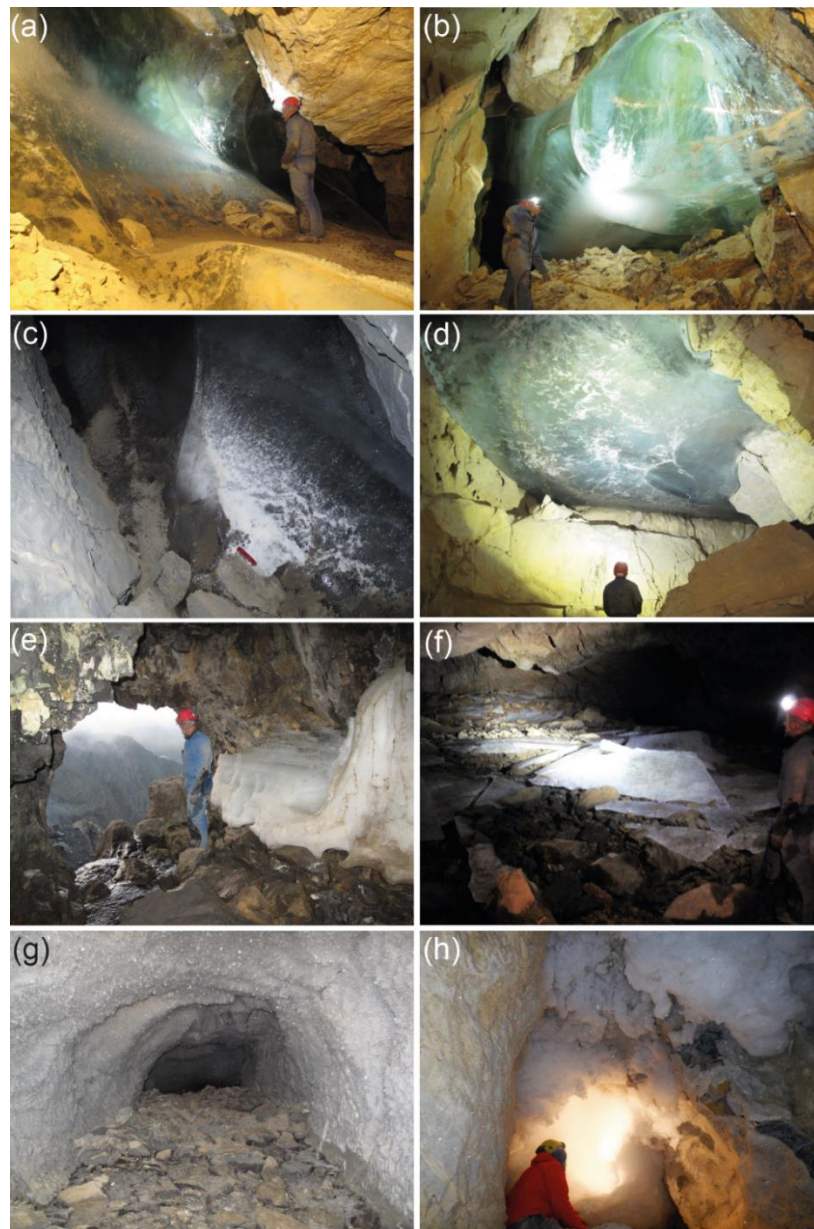


Figure 6. (a) Upper part of the ice body in room D. (b) Ice body hanging from the ceiling and the southwest wall in room G. White spots near the bottom of the deposit correspond to air inclusions as well as cryogenic carbonates and gypsum in the ice. (c) Small ice body in room SPD with CCC-CCG on and within the ice. Red knife (9 cm) for scale. (d) Ice body on the ceiling of room K (Terminus Devaux, TD). (e) Brulle spring and remains of a layered ice body (September 2018). (f) Broken ice sheets in the flooded area in room F (September 2018). (g) Millimetre to centimetre size perennial hoarfrost in a blind gallery below SPD room. (h) Seasonal hoarfrost aggregates (>30 cm long size) covering a cupola close to room J.

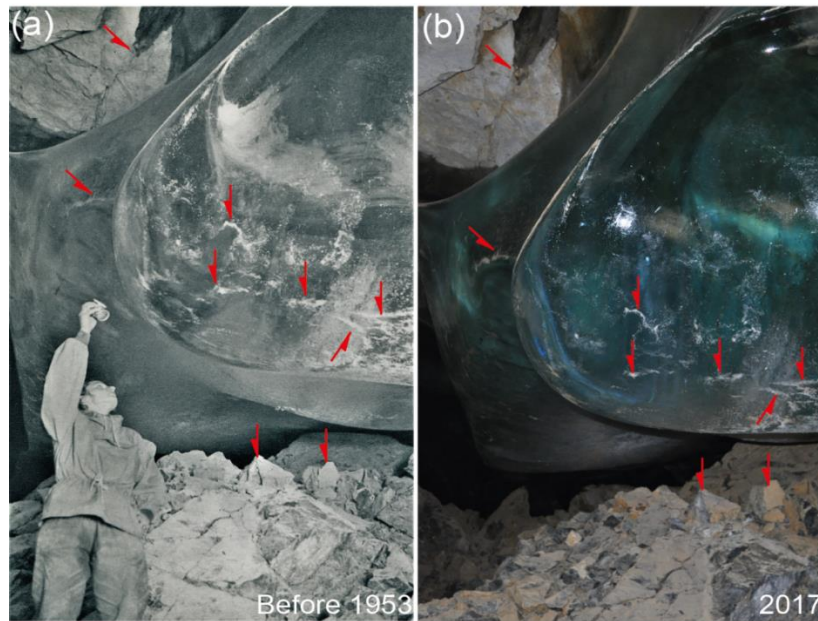


Figure 7. (a) Photo of the ice body located in room G taken shortly before 1953 (Casteret, 1953). (b) Photo taken in 2017. In both pictures, white patches on the ice surface correspond to small CCC accumulations released from the ice by sublimation. Red arrows indicate common features in both images.

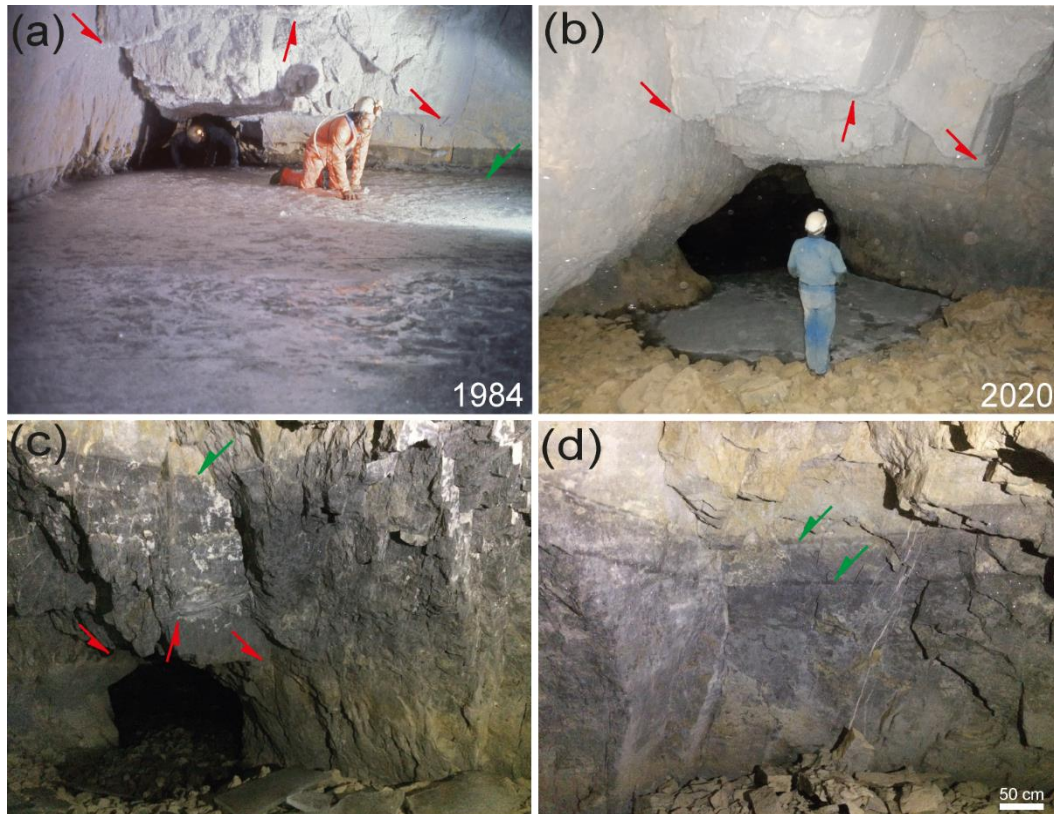


Figure 8. (a) Photo taken close to the river sector that connects the rooms F and E. The estimated ice level is 5 m higher than the Brulle spring. Photo by Jean Luc Bernardin (8<sup>th</sup> August 1984). (b) Similar area in 2020, and maximum extension of the seasonal lake ice formed during winter. (c) Higher ice mark level (c. +9.5 m with respect to the Brulle spring) and remnants of ice sheets from the frozen lake in 2018. (d) Two ice level marks (c. +9.2 m and +8.8 m with respect to the Brulle spring) located between the highest mark and the elevation of the ice in photo (a). In all images red arrows indicate the same rock edges, while green arrows show ice-level marks.



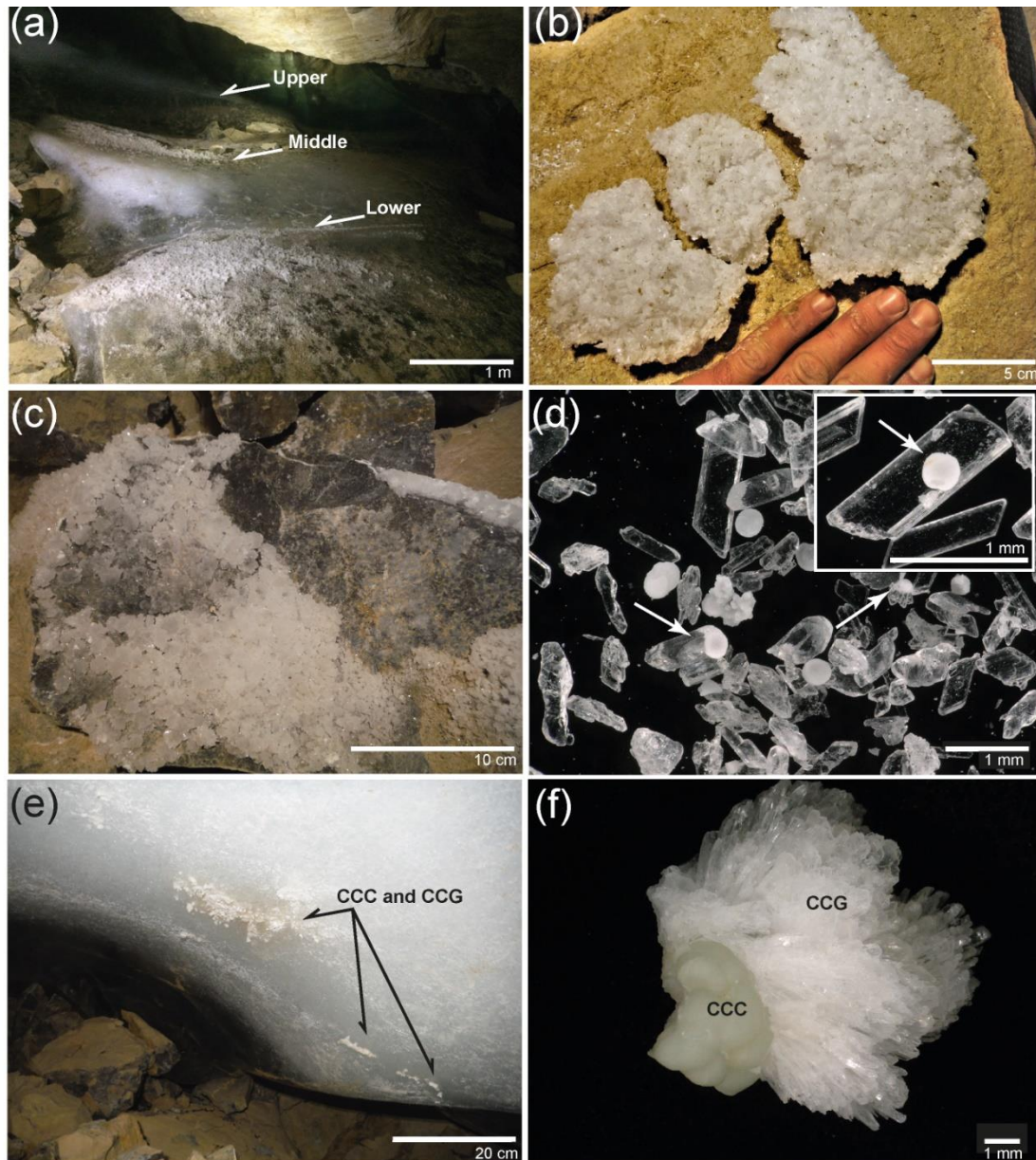


Figure 9. (a) Ice body in room G and three levels marked by cryogenic gypsum partially still in situ in the ice. The white area corresponds to milky ice with a high abundance of air inclusions. Gypsum crystals cover parts of the surface of the ice body due to ice retreat. (b) Large gypsum “raft” deposited on a block in room D. (c) Block in room D with gypsum overgrowths. (d) Microscopic image of euhedral CCG with cores of CCC (white arrows), globular CCC, and enlarged image of euhedral gypsum crystal with a nucleus of globular CCC. (e) CCC and CCG entrapped within milky ice in room G. (f) Detail of a CCC sample from room G covered by CCG.



Date	Sample	Cations					Anions									
		Na <sup>+</sup>	NH <sub>4</sub> <sup>+</sup>	K <sup>+</sup>	Ca <sup>2+</sup>	Mg <sup>2+</sup>	F <sup>-</sup>	Cl <sup>-</sup>	NO <sub>2</sub> <sup>-</sup>	Br <sup>-</sup>	NO <sub>3</sub> <sup>-</sup>	SO <sub>4</sub> <sup>2-</sup>	HCO <sub>3</sub> <sup>-</sup>	CO <sub>3</sub> <sup>2-</sup>	PO <sub>4</sub> <sup>3-</sup>	
15/09/2017	Devaux river 1	1.6	0.0	0.5	36.0	8.5	0.0	0.2	0.0	0.0	0.0	1.8	21.6	61.0	11.6	0.0
	Devaux drip 1	0.9	0.1	0.5	50.5	18.2	0.1	0.5	0.0	0.0	6.8	67.4	95.2	0.0	0.0	0.0
	Devaux drip 2	1.4	1.2	1.3	53.2	19.5	0.1	1.1	0.1	0.0	7.4	70.1	101.3	0.0	0.0	0.0
22/07/2018	Devaux Ice 1 (room D)	2.3	0.0	0.3	24.8	2.7	0.1	1.3	0.0	0.0	0.7	19.0	23.9	1.0	0.0	0.0
	Devaux Ice 2 (room D)	2.2	1.3	2.5	27.8	2.0	0.0	2.1	0.0	0.0	1.5	17.0	30.7	0.0	0.0	0.0
	Devaux river 1	0.6	0.0	0.4	32.4	4.4	0.0	0.2	0.0	0.0	0.9	5.1	53.7	4.0	0.1	0.0
22/09/2018	Devaux river 2	0.6	0.0	0.4	32.2	4.4	0.0	0.2	0.0	0.0	0.9	5.1	56.1	2.6	0.0	0.0
	Devaux drip 1	1.4	0.0	3.2	61.0	20.8	0.2	2.2	0.0	0.0	14.1	76.0	84.2	5.6	0.0	0.0
	Devaux drip 2	2.3	0.1	1.7	60.8	21.0	0.2	2.2	0.0	0.0	14.1	76.9	91.5	4.4	0.0	0.0
28/07/2020	Devaux river 1*	1.3	0.0	0.4	40.5	7.9	0.0	0.3	0.0	0.0	2.0	17.0	65.9	0.0	0.0	0.0
	Devaux drip 1*	1.6	0.0	1.2	70.6	27.2	0.2	1.1	0.0	0.0	19.8	116.5	90.3	0.0	0.0	0.0
	Devaux ice (seasonal)*	0.4	0.0	0.5	28.2	1.1	0.1	0.5	0.0	0.0	0.5	2.8	36.6	0.0	0.0	0.0
26/07/2021	Devaux river 1*	0.6	0.0	0.3	31.5	4.1	0.0	0.2	0.0	0.0	0.8	5.9	58.6	0.0	0.0	0.0
	Devaux drip 1*	1.1	0.2	1.1	42.3	12.5	0.1	0.5	0.0	0.0	2.9	38.4	101.3	0.0	0.0	0.0
	Devaux drip 2*	1.1	0.1	1.0	43.6	13.5	0.1	0.4	0.0	0.0	2.7	38.2	89.1	0.0	0.0	0.0
13/08/2021	Devaux drip 3*	1.6	0.7	1.5	47.9	13.1	0.1	1.1	0.0	0.0	2.2	36.7	107.4	0.0	0.0	0.0
	Devaux drip 1	2.9	0.0	1.1	83	35.9	0.3	5.9	0.6	0.1	40.2	269.3	104.9	0.0	0.0	0.0
	Devaux drip 2	3.3	0.4	2.0	73.2	29.3	0.2	6.0	0.1	0.0	28.6	212	112.2	0.0	0.0	0.0
26/07/2021	Devaux river 1	0.4	0.0	0.1	25.7	4.3	0.1	2.6	0.1	0.0	3.2	16.3	68.3	0.0	0.0	0.0
	Devaux river 1	0.7	0.0	0.2	28.6	4.9	0.1	2.6	0.0	0.0	1.5	20.4	74.4	0.0	0.0	0.0
	Devaux drip 1	7.5	2.2	5.1	49.5	15.2	0.2	10.3	0.3	0.0	6.9	77.3	130.5	0.0	0.0	0.0
26/07/2021	Devaux drip 2	5.1	1.3	2.8	49.3	15.6	0.2	6.5	0.1	0.0	6.5	80.5	129.3	0.0	0.0	0.0

Table 1. Chemical composition of water and ice samples from Devaux cave (in mg/l). \* Samples where TDS (total dissolved solids) was calculated.

<b>Location</b>	<b>Sample and description</b>	<b><math>\delta^{34}\text{S}</math> (‰) VCDT</b>
Room D	Gypsum crystal (part of large raft)	-15.8
Room D	Gypsum crystal (part of large raft)	-15.5
Room D; lower gypsum level	Gypsum crystal (individual)	-15.6
Room D; middle gypsum level	Gypsum crystal (individual)	-15.0
Room D; middle gypsum level	Gypsum crystal (individual)	-15.6
Room D; upper gypsum level	Tiny gypsum crystals (aliquot)	-15.3
Room D	Gypsum crystal (individual)	-15.1
Room G	Gypsum crystal (individual)	-12.3
Room G	Gypsum overgrowth (individual)	-12.1
Room G	Gypsum overgrowth (individual)	-11.9
Room G	Gypsum overgrowth (individual)	-12.1
Room G	Gypsum overgrowth (individual)	-12.0
Limestone above cave	Pyrite crystal (individual)	-12.7
Entrance "Porche"	Drip water (1 liter)	-14.4
Brulle spring	River water 1 (1 liter)	-28.5
Brulle spring	River water 2 (1 liter)	-27.3

Table 2. Sulfur isotope values of gypsum, water and pyrite from Devaux.